UC San Diego
UC San Diego Electronic Theses and Dissertations

Title
A Study of Droplet Impact on Liquid Film Using Two-Liquid Systems

Permalink
https://escholarship.org/uc/item/4v68958s

Author
wu, xian

Publication Date
2020

Peer reviewed|Thesis/dissertation

UNIVERSITY OF CALIFORNIA SAN DIEGO

A Study of Droplet Impact on Liquid Film Using Two-Liquid Systems

A thesis submitted in partial satisfaction of the
requirements for the degree
Master of Science

in

Engineering Science (Applied Ocean Science)

by

Xian Wu

Committee in charge:

Professor Abhishek Saha, Chair
Professor Jinhye, Bae
Professor James R Friend

2020

The thesis of **Xian Wu** is approved, and it is acceptable in quality and form for publication on microfilm:

_____

_____

_____

Chair

University of California San Diego

2020

To the year of 2020.

EPIGRAPH

You would never know if a drop fell in the water. If you didn't see the ripples.

—James John

TABLE OF CONTENTS

LIST OF FIGURES

viii

LIST OF TABLES

List of Symbols

$A_{0,f}$	initial surface area of the film before the deformation
$A_{0,d}$	initial surface area of the droplet before the deformation
$A_{max,f}$	surface area of the deformed film at the maximum spread
$A_{max,d}$	surface area of the deformed droplet at the maximum spread
ΔA_f	surface area difference in the film between $A_{max,f}$ and $A_{0,f}$
ΔA_d	surface area difference in the droplet between $A_{max,d}$ and $A_{0,d}$
ΔA^*	surface area ration between ΔA_f and ΔA_d
C	height of the droplet's center captured from the side-view
C_{cap}	constant in the capillary time scale
E_0	initial energy of the rebounding process
$E_{kd,0}$	initial kinetic energy of droplet
$E_{kd,p}$	kinetic energy of droplet in the penetration process
$E_{kd,r}$	kinetic energy of droplet in the rebounding process
$E_{kf,p}$	kinetic energy of film in the penetration process
$E_{kf,r}$	kinetic energy of film in the rebounding process
$E_{\phi,f}$	viscous dissipation of film (in total)

$E_{\phi,f,1}$	viscous dissipation of film along the cylindrical side surface
$E_{\phi,f,2}$	viscous dissipation of film along the semi-sphere bottom surface
$E_{\phi,d}$	viscous dissipation of droplet
g	gravitational acceleration
$G(x,y)$	2-dimension Gaussian filter
$H(x,y)$	processed image
H	the thickness of the liquid film in the chamber
H^*	the dimensionless parameter of the film thickness
H_p	the penetration depth measured by the deformation of the film
H_p^*	the dimensionless parameter of penetration depth
H_{pm}	the maximum penetration depth measured by the deformation of the film
H_{pm}^*	the dimensionless parameter of maximum penetration depth
$H_{pm,e}^*$	the dimensionless parameter of experimental maximum penetration depth
$H_{pm,a}^*$	the dimensionless parameter of analytical maximum penetration depth
H_d	the height of the droplet at the maximum spread
$I(x,y)$	raw image
k	wave number
n	normal vector to the detected boundary
Oh_f	the Ohnesorge number of the film
Oh_d	the Ohnesorge number of the droplet
R	initial radius of the droplet
r	radius in the flow field of the film
r_1	bottom radius of both the film and droplet at the maximum spread

r_2	top radius of the film at the maximum spread
r_3	top radius of the droplet at the maximum spread
r_4	vertical radius of the droplet at the maximum penetration depth
r_5	horizontal radius of the droplet at the maximum penetration depth
r_{45}^*	the spread ratio between r_4 and r_5
$(\Delta SE)_f$	Surface energy of the film
$(\Delta SE)_d$	Surface energy of the droplet
Δt	retracting time in the late merging case
t_{cap}	capillary time scale
u_f	rebounding velocity of the film
u_d	rebounding velocity of the droplet
U^*	rebounding velocity ratio between u_f and u_d
U_{crit}^*	critical rebounding velocity ratio between different impact outcomes
U	impact velocity of the droplet
U_0	initial impact velocity of the droplet from the linear fitting
U_1	instant impact velocity of the droplet from the image processing
U_p	penetration velocity of the droplet
$U_{p,a}$	penetration velocity by scaling analysis
$U_{p,e}$	penetration velocity from experiment
$U_{p,min}$	minimum penetration velocity from experiment
$\overline{U_p}$	averaged penetration velocity
U_f	velocity of the film in the penetration process
V	volume scale in the calculation of viscous dissipation

We	the Weber number
w_1^*	the spread ratio between r_1 and R
w_2^*	the spread ratio between r_2 and R
w_5^*	the spread ratio between r_5 and R
ρ	density of the liquid
ρ_f	density of the film liquid
ρ_d	density of the droplet liquid
σ	surface tension of the liquid
σ_f	surface tension of the film liquid
σ_d	surface tension of the droplet liquid
ν	kinetic viscosity of the liquid
ν_f	kinetic viscosity of the film liquid
ν_d	kinetic viscosity of the droplet liquid
μ	dynamic viscosity of the liquid
μ_f	dynamic viscosity of the film liquid
μ_d	dynamic viscosity of the droplet liquid
ϕ	viscous dissipation rate scale
ϕ_f	viscous dissipation rate in the film
ϕ_d	viscous dissipation rate in the droplet
δ	boundary layer thickness
η	parameter in the maximum spread model
ω_{cap}	undamped capillary wave frequency

ACKNOWLEDGEMENTS

I would like to thank Professor Abhishek Saha for his support as the chair of my committee. Through the past one and half years research, his guidance has proved to be invaluable. I also would like to thank Professor James R. Friend and Professor Jinhye Bae for their support as the member of my committee.

Thanks to all the dear friends in my lab and my family. Especially in this year of 2020, it is their support that helped me to take what have happened till now.

ABSTRACT OF THE THESIS

A Study of Droplet Impact on Liquid Film Using Two-Liquid Systems

by

Xian Wu

Master of Science in Engineering Science (Applied Ocean Science)

University of California San Diego 2020

Professor Abhishek Saha, Chair

Droplet impact on liquid film is of critical importance in several industrial applications, such as inkjet printing and thermal sprays. Single-liquid system (same liquid for the droplet and the liquid film) has shown two outcomes for the impact of a droplet on a liquid film, namely bouncing and merging. The transition between the regimes of bouncing and merging has been reported to be a function of the impact

Weber number and the film thickness. Very often, in practical application such as in multiple layer 3D printing, the droplet and liquid film are composed of different liquids. Thus, a good understanding of the droplet impact dynamics in two-liquid systems (i.e. different liquid for the droplet and the film) is required to control these processes. However, very few studies in literature have focused on two-liquid systems. In this thesis, we experimentally investigate the dynamics of droplet impact in a two-liquid system with contrasting liquid property ratios. Experimental observations from the two-liquid systems show a significant shift in the transitional boundaries, where droplet impact outcomes change from bouncing to merging, with respect to that of the single-liquid system. In addition to the two types of merging of the droplet to the liquid film, early merging and late merging, reported for single-liquid systems, we also observe a new type of merging for two-liquid systems. Additionally, the findings from experiments have also been reproduced using theoretical analysis.

Chapter 1

Introduction

Situations in which droplets with variable size move and impact with another object or surface often happen in natural and industrial world. The outcome of the droplet impact is playing the most important role in various physical processes, such as combustion, printing, surface coating and other manufacturing methods.

In order to understand the mechanism behind the outcome of droplet impact, many studies have been done both experimentally and theoretically. Here, in this thesis, the impact outcomes from the droplet impact on liquid film in both single-liquid systems and two-liquid systems are presented and discussed.

1.1   Background

Among engineering applications that involve the impact of droplets, the outcome of the impact of a droplet on a solid or liquid surface is very important. Splashing, jetting, and bouncing are some of the most common outcomes of droplet impact.

Understanding the mechanism of each of these outcomes is crucial in order to control the impact outcomes in industrial applications. One important process that is highly affected by the impact of droplet on a wet or dry surface is inkjet printing.

Inkjet printing is a technology where text and images are printed onto a porous surface. In the printing process, the ink is always in the form of a droplet that impacts on a target surface (mostly a solid surface). Inkjet printing can also be done layer by layer to contract a 3D model, a process commonly known as 3D printing, or additive manufacturing (AM). Wang et al.[1] reviewed the common 3D printing technique including the inkjet 3D printing. In inkjet 3D printing, also known as powder-liquid 3D printing, a liquid droplet will land on a layer of powder, spreading in a designed position in each layer. Many factors in the droplet impact process affect the quality of the final products, such as the size of the droplet, the viscosity, and interaction between the droplet and the powder layer.

Calvert[2] reviewed different inkjet printing techniques that uses a wide range of materials and concluded various outstanding issues that affects the interaction of the ink with the substrate. Specifically, in multiple layer printing, due to different drying time for each layer, re-dissolution, re-suspension or re-melting will occur in between each layer. This is one of the major challenge in controlling the printing of multiple layers in such a process. Each of these layers mix and form discrete unmixed layers.

Another interesting application that involves droplets is the thermal sprays to generate thermal barrier coating that are widely used in modern gas turbine engines to decrease the heat transfer to the metal surface. The key technique used for the application of the coating is a thermal spray. Feuerstein et al.[3] reviewed the major

2

elements of thermal sprays such as material, equipment and processing. To get a better understanding of how the micro-structure of spray coating depends on the operation condition, Mostaghimi et al.[4] developed a model for the high velocity oxy-fuel spray coating process. This model considers both the effect of different spray parameters such as particle size, temperature, velocity and impact points, on the quality and characteristics of the surface coating. As the former droplet impacts and deforms into a splat, the following droplet would impact onto the splat instead of the original solid surface. Here, they used a simple disc-shape spread model developed by Aziz and Chandra[5] which neglects splashing and break-up.

Among all these applications, the impact of droplet serves as a process to transfer the required information. If the outcome of the droplet impact remains out of control, the efficiency of related application can not be ensured. For instance, in the thermal spray model, many problem will occur when splashing happens as the system is designed to fit the non-splashing model. Hence, to understand and control the impact outcomes are of crucial importance.

1.2 Droplet Impact Phenomenon

1.2.1 Methodology

To study the droplet impact phenomenon, several methods are used both experimentally and analytically. Before the advent of high speed imaging, manual observations were used to study droplet impact [6]. Current experimental investigations involve high speed imaging [7], shadowgraphy [8], interferometry[9], Particle

Image Velocimetry (PIV) [10] to study the flow fields, Laser Induced Fluorescence (LIF) [11]to study mixing, tomography to study dynamics of droplet clouds etc. One can also study the dynamics of droplet using high fidelity numerical simulations [12].

Worthington[6] was one of the pioneers who reported experimental observations of impacts of a liquid droplet on a solid surface. He studied patterns left by the droplet's impact on a solid surface. A manual observation method was used where a stroboscopic light is used to illuminate the droplet as it impacted the solid surface which left a visual memory of the shape of the droplet impact. Several drawings were shown to describe how the impact patterns form and grow.

With the growth of high speed imaging technology, scientists can now observe the impact phenomena in a very detailed manner. Thoroddsen et al.[13] provides a detailed review of high speed imaging techniques used to study droplets and bubbles.

Apart from the experimental approaches, many studies analyze droplet impact analytically or numerically. Many modeling ([14], [15], [16]) have been done in the droplet impact on solid surface by using the energy balance between the initial kinetic energy of the droplet, surface energy and the viscous dissipation. However, these models lack of detailed information like pressure or velocity during the deformation of the droplet[17]. Harlow and Shannon[18] numerically solved the full Navier-Stocks equation in cylindrical coordinates to investigate the splash resulting from an impact of a droplet on a flat plate.

1.2.2   Droplet Impact on Solid Surface

Droplet impact on dry surfaces has been well studied because of its relevance in with printing and coating. Josserand and Thoroddsen[19] gives a detailed review of various studies on impact of a droplet on a solid surface. Three outcomes of impact was reported, namely deposition, bouncing and splashing. They remarked that even a very thin layer of liquid film can cause a significant change in impact outcomes.

Power-law boundary relations were formulated by Vander Walto et al.[20] to delineate the splash and non-splash regimes of impact on dry surfaces or thin films under isothermal conditions, using the Ohnesorge and Reynolds numbers.

Some of the studies focus on the different outcomes of droplet impact caused by contrasting nature of the impact surfaces. Hydrophobic surfaces are commonly used to study the droplet impact mechanism. Bartolo et al.[21] discovered that when water droplets gently impact on a hydrophobic surface, the droplet shoots out a violent jet. Alternatively, a superamphiphobic coating surface was used by Xu Deng et al.[22]. They observed multiple different impact modes such as rebounding, partial or full pinning, or splashing by changing the inertia of the droplet and the capillarity of the impact surface. By comparing different ethanol-water and glycerin-water droplets, two retraction modes of the film post droplet impact were discussed where the surface energy mainly transfers the kinetic energy of the film. Lastly, Antonini et al.[23] studied the droplet impact phenomenon on different surfaces ranging from hydrophilic to superhydrophobic.

Smith and Bertola[24] measured the fluid velocity inside the impacting droplets using particle image velocimetry (PIV). The velocity of the fluid inside the droplet

was expressed as a function of time and the radial position. By comparing this velocity function for water droplet with a 200 *ppm* polyethylene oxide droplet, they identified extensional viscosity as the main factor that determine the anti-rebound effect during both the spreading and the rebounding processes.

1.2.3 Droplet Impact on Liquid Surface

Beyond solid surfaces, considerable studies have focused on the droplet impacting on a liquid film (however, in single liquid system). Yarin[25] provides a review of the outcomes of droplet impact on liquid films. Several impact outcomes, such as crown formation (splashing), drop spreading, jetting and fingering were identified.

Pan and Law[26] investigated the head-on collision of drop impact on same liquid film. The transition from bouncing, which means the drop is absorbed by film in certain impact Weber number, to merging is mainly studied both experimentally and computationally. The impact behavior was explained, and the impact results were summarized with the change in impact Weber number and the film thickness.

Tang et al.[27] used more experimental data to show the impact outcome regime graph, with respect to different liquid. The impact outcomes were divided into bouncing, early merging and late merging because of different impact Weber number and the film thickness. Also, the viscosity effect on the impact result was discussed in the impacting model with the energy balance. Thus each transition limits were explained with the dependence on impact Weber number or film thickness.

Harlow and Shannon[18] numerically solved the full Navier-Stock equation in cylindrical coordinate to investigate the splash of droplet impact on a flat plate,

into a shallow pool or into a deep pool. Marie-Jean Thoraval et al.[28] discussed the splashing resulting from the droplet impact on a liquid pool in detail. The microdroplets generating from the splash were traced by ultrahigh-speed imaging and high-resolution simulation of the impact process. Cossali et al.[29] studied the splashing of a droplet when it impacts on a thin film through experiments. They observed that the film thickness does not have a strong influence over the splashing process. The impact Weber number controls the crown height, whereas the growth rate of the crown is independent of the impact Weber number. Jae Bong Lee et al.[30] concluded that in dry and wet surfaces the liquid properties, namely viscosity and surface tension, showed a direct effect on the maximum spreading ratio of the impacting drop. Berberović et al.[31] investigated the crater formation experimentally, numerically, and theoretically. The drop inertia, viscosity, gravity and surface tension all play an unignorable part in crater formation.

There are very few investigations on the impact of droplet in a two-liquid system. However, a conclusive understanding of the impact outcome is still elusive. Antonini et al.[23] studied the dependence of rebounding time on the surface contact angle. They found that the drop rebounding process is mainly affected by the receding angle. Wang et al.[32] theoretically analyzed the balance of interfacial tension in drop impact onto an oil layer. Along the triple-line, the interfacial tension balance is well maintained because of a low capillary number. Droplet penetration processes was simulated numerically to understand the transition between the regime of non-penetration and penetration. A semi-empirical model was used to obstain the critical penetration distance as a function of the spread ratio, which has a weak dependence

on the ratio of viscosities.

1.3   Thesis Objectives

The transition limits of the outcome of impact of a droplet on a solid surface or on liquid films, in single-liquid systems, has been investigated in detail in the past. Even though many studies have been conducted to identify the nature of the impact of a droplet on a liquid film consisting of same liquid, the regime map for the impact outcomes in a 2-liquid system is not well explored. With a relative change in liquid properties of film and droplet, one can observe a significant shift in the transition boundaries between regimes of different impact outcomes. The primary objective of this thesis is to experimentally investigate the outcomes of the impact of a liquid droplet onto a liquid film composed of a different liquid (2-liquid system). We also perform a theoretical analysis to compliment the experimental findings, and discuss the role of different liquid properties in determining the outcomes of the impact of droplet on a liquid film through a scaling analysis.

1.4   Organization of the Thesis

This thesis is divided into 4 chapters: Introduction, Experimental Methods, Results and Analysis, and Discussion.

In this chapter (introduction), we discussed some relevant applications and studies on the droplet impact phenomenon. Further, we presented a detailed introduction to various studies on the impact of droplets on different types of surfaces (solid,

porous or liquid). Chapter 2, titled Experimental Method, explains the design of the droplet impact experiment used in this thesis. The chapter 3, titled Experiment Results and Analysis, presents the observations from the droplet impact experiments and describes the scaling analysis corresponding to each transition boundaries in the impact regime graph. A new type of merging phenomenon is also introduced and discussed. The last chapter provides the conclusions from both the experimental findings and scaling analysis. Further, we also discuss possible extensions to the present work. Moreover, an appendix is provided with additional figures to show the complete work done of this thesis.

Chapter 2

Experimental Method

In this chapter, we introduce how to experimentally investigate the event where droplets impact on a liquid film both in single-liquid systems and two-liquid systems. When the droplets impact onto a liquid film, the impact result may vary from *bouncing* to *merging* depending on many factors, such as droplet initial energy, the thickness of liquid film and the liquid proprieties (both for droplet and the film). Our objective is to observe and understand the different regimes of the impact outcomes. We first present an overview of our experimental approach to observe the outcomes of droplets impacting on liquid films.

2.1   Experimental Setup

Figure 2.1 shows the schematic diagram of the experimental setup. The main components are (1) a syringe pump and needle to generate and release the droplet, (2) a transparent cubic glass chamber which contains the liquid film on a flat surface
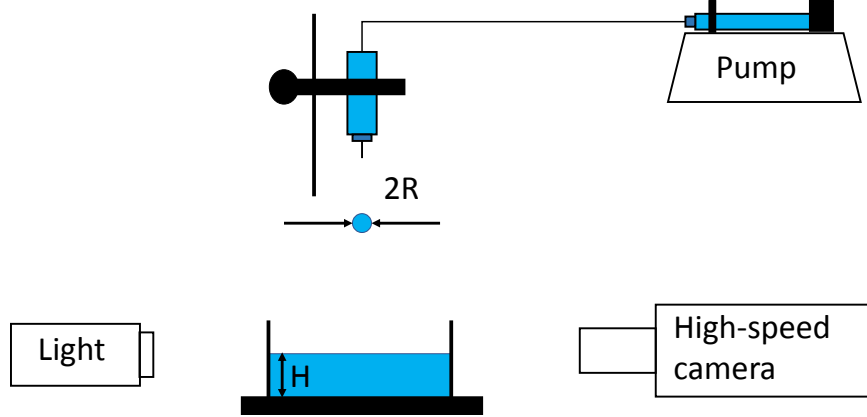
Figure 2.1: The schematic diagram of the experimental setup used for the droplet impact study. Droplet is created by pushing the liquid through a blunt needle of size 0.03 mm using a syringe pump.

(3) an vertical translational stage on which the needle is fixed, (4) a monochromatic high-speed camera (Phantom V7.3) with a 50 mm Nikon lens and an extension bellow to record the impact process at a rate of 15000 frames per second (figure 2.2), (5) a diffused light to provide background illumination for shadowgraphy.

A droplet (with a radius R) is formed by forcing the liquid from the syringe pump at a constant flow rate. The flow rate is low enough to ensure that the droplet is generated at the tip of the needle and it gets detached from the needle due to gravity. To ensure the repeatability, the entire connection between the syringe and the needle is filled with the liquid without any trapped air bubbles.

As introduced in the former section, the outcome of droplet impact on liquid film is controlled by the droplet impact velocity U, the thickness of the liquid H, and the liquid proprieties. In the experiment, the droplet impact velocity is only controlled

by the initial height from which the the droplet is released, since the droplet is released under its own weight. As for the film thickness, we can easily control it by controlling the volume of the liquid in the cubic glass chamber. Since here we are investigating the influence of the liquid proprieties on the impact outcomes, to get a set of different droplet and film liquid property ratios, five different liquids with nine droplet-film combinations are used in the experiment. The properties of the different liquids used in the experiments are provided in table 2.1.

It is essential to ensure the repeatability of the impact outcomes since any unexpected factor can cause a change in the experimental result. Therefore, the experiments were repeated at least three time under the same conditions (liquid combination, initial height and film thickness). To keep the liquid free of dust particles, the glass chamber and the needle are regularly cleaned with acetone and air flow after and before every experiment. To ensure that the droplet impacts on a flat liquid surface (rather than a curved part of the meniscus), the needle is vertically aligned with the center of the chamber. To ensure the accuracy of the length scale in the image, calibration is done every time before the experiment. Also, both the camera and the surface which holds the chamber are checked to be horizontal before the experiment.

2.2   Image Processing

Image processing technique, in effect, is a filtering technique that choose certain required data from the image[33]. It allows us to convert the raw image recorded

Table 2.1: The properties of different liquids used in the experiment

Liquid	Density ρ (kg/m^3)	Surface Tension σ (N/m)	Kinetic Viscosity ν (cSt)
C10	730	0.02455	2.37
C14	767	0.0265	3.6
S3	898	0.0183	3
S4.5	898	0.01816	4.5
S20	950	0.0207	20

from the camera (an array of pixels, each with a brightness or the color information) to a modified image that emphasizes some required feature. Here, in our experiment, the boundary between the droplet and the air is needed to calculate the droplet's initial radius and the impact velocity. We perform an edge detection to obtain this boundary.

Many edge detectors has been developed from the basic idea to locate the local boundary information by thresholding and skeletonizing the pixel-intensity variation map[34]. Among the well developed edge detection algorithms, such as Canny detector, Gauss-Laplace detector, Kirsch detector and Robert detector, Canny algorithm has been widely used because of its good performance in detecting the boundary[35]. Thus, in this work, we choose to use Canny edge detector to identify the droplet boundary from the raw image.

The optimality of the Canny detector is ensured by the following three criteria[36]:

(a) The detection criteria ensures that there no missed edges and no spurious responses.

(b) The localization criteria ensures that the distance between the actual edge and the detected edge is minimum.

(c) The one response criteria ensures that a unique edge is detected even when
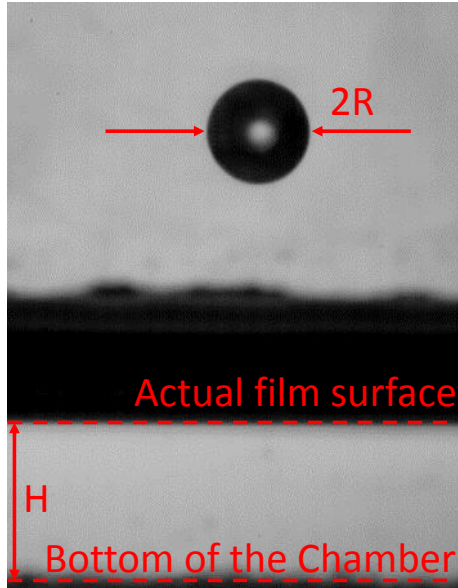
Figure 2.2: Side-view of the droplet impact on liquid film from experiment. Droplet is a sphere with a radius R. The thickness of film H is measured from the bottom of the chamber to the film surface where the deformation can be measured in the side-view.

the noise in the image causes the gradient of intensity at a boundary to have multiple maxima in the vicinity of the edge.

For the raw image $I(x, y)$ obtained from the experiment, there exists a symmetric 2-dimension Gaussian filter $G(x, y)$ that meets the above three criteria[37]. The processed image $H(x, y)$ can then be obtained as:

$$H(x, y) = G(x, y) * I(x, y) \tag{2.1}$$

Suppose n is the normal vector to the detected boundary, then the n can be

expressed as:

$$n = \frac{\partial H/\partial n}{|\partial H/\partial n|} \qquad (2.2)$$

According to the localization criteria, the edge location should identify the local maximum of the first derivative of $H(x, y)$ in the normal direction n. In another words, it locates those points in $H(x, y)$ where the second derivative of $H(x, y)$ crosses zero, as shown in eq 2.3.

$$\partial^2 H/\partial n^2 = 0 \qquad (2.3)$$

From this point of view, the local maxima can be found in the normal direction to the edge. This approach is also known as non-maximal suppression NMS). Often, after the NMS operating, there exists some spurious responses, which is so called 'streaking' problem. This streaking problem is common in the edge detecting process and can be eliminated by applying a threshold. Thus, by setting the proper threshold, the experiment images are processed to calculate the droplet initial radius, the droplet instant velocity and etc. Here, by tracing the displacement of droplet C in each frame and recording the actual time t by the frame number, the instantaneous velocity of the droplet U_1 is calculated as:

$$U_1(t) = \frac{(C(t_n) - C(t_{n-1}))}{(t_n - t_{n-1})} \qquad (2.4)$$

However, from the side view there exist a shadow region above the actual film surface due to the curvature of the meniscus of the liquid film, which hinders the tracking of the droplet using boundary detection in this region. To account for this

15

effect, we extrapolate the droplet velocity U as a linear function of time with the acceleration due to gravity as the constant of proportion:

$$U = U_0 + g * t \tag{2.5}$$

As shown in figure 2.3, the instantaneous velocity is increases linearly with time with a slope equal to acceleration due to gravity, g.
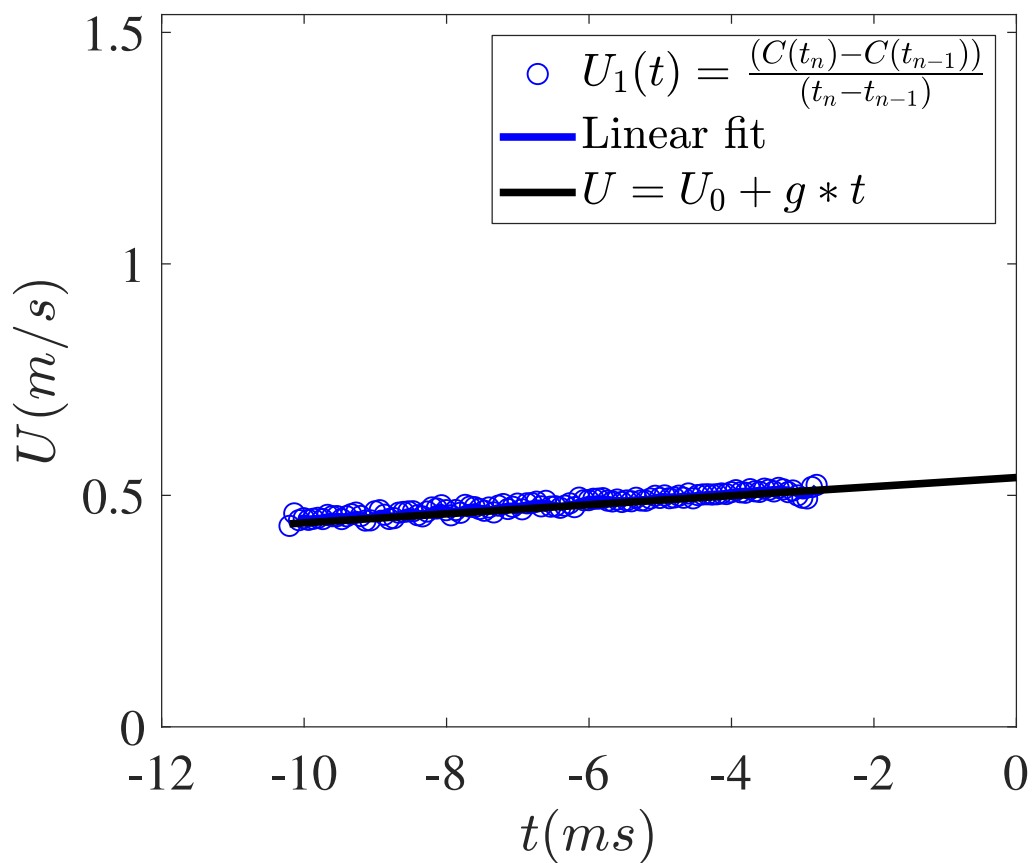
Figure 2.3: Droplet impact velocity extended as a linear function of impact time. Impact time t is from the moment when droplet can be entirely captured in the side-view till the last moment when the film remains undisturbed.

Chapter 3

Results and Discussion

3.1   Impact of droplet on liquid films

3.1.1   Single-liquid System

Droplet impact on a liquid film in the single liquid system, where liquids that constitute both the drop and the film are the same, has been well discussed in former studies. Fig 3.1 shows time-resolved side-view snapshots of three typical impact outcomes in the single-liquid system, namely, *bouncing*, *early merging*, and *late merging*. In the impact process, for a given liquid, the initial kinetic energy and the film thickness play the dominating roles in determining the outcome of the impact. The dimensionless parameters corresponding to the initial kinetic energy of the droplet and the film thickness are the droplet Weber number defined as $We = \frac{2\rho_d RU^2}{\sigma_d}$ and the dimensionless film thickness defined as $H^* = \frac{H}{R}$.

At low We and high H^* (figure 3.1.a), the droplet impacts and deforms the film

We=16.55 H*=2.27

(a)

t = 1.33ms   4.67ms   8ms   11.33ms   14.67ms

We=17.67 H*=2.19

Merging

(b)

t = 0.67ms   1.33ms   1.67ms   2ms   2.33ms

We=15.25 H*=0.85

(c)

t = 2.67ms   4.33ms   6ms   7.67ms   11ms

We=16.29 H*=1.76   Merging

(d)

t = 1ms   2.67ms   6ms   9.33ms   9.67ms
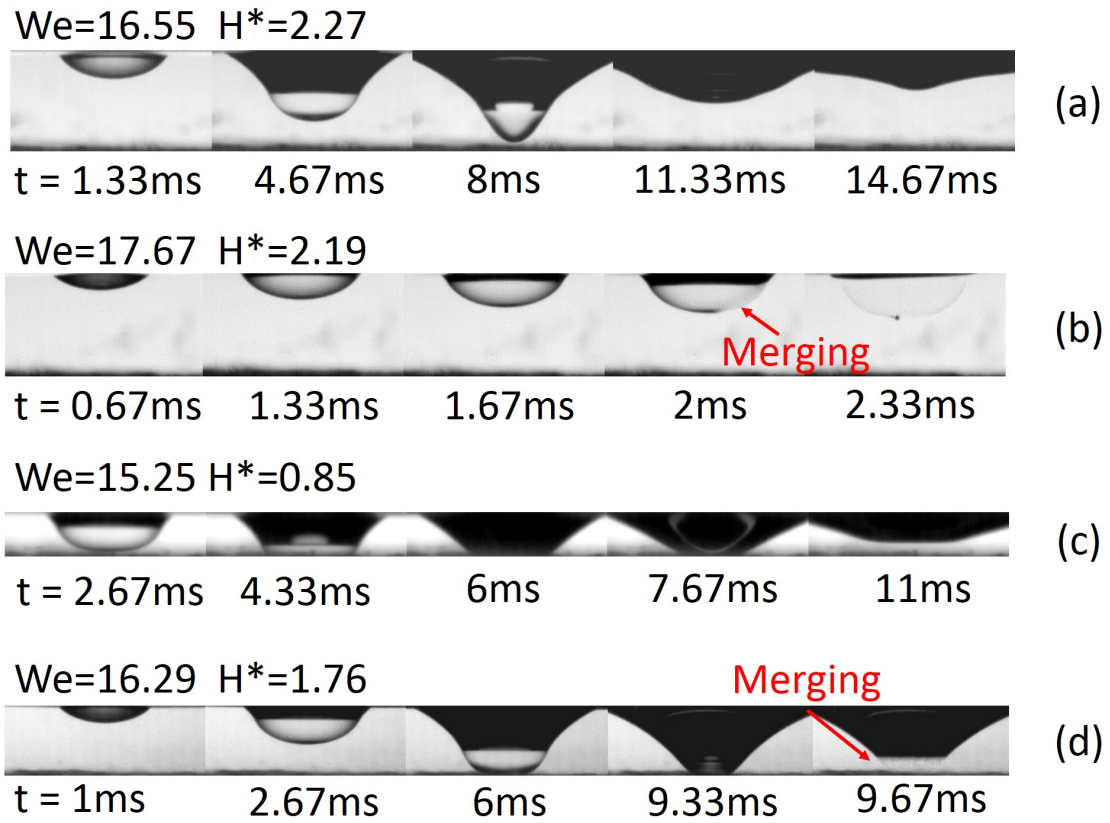
Figure 3.1: The side view of different impact outcomes from droplet impact on a liquid film experiment in a single-liquid system. (a)Bouncing on a deep pool.(b)Early merging on a deep pool.(c)Bouncing on a shallow pool. (d)Late merging on a shallow pool.
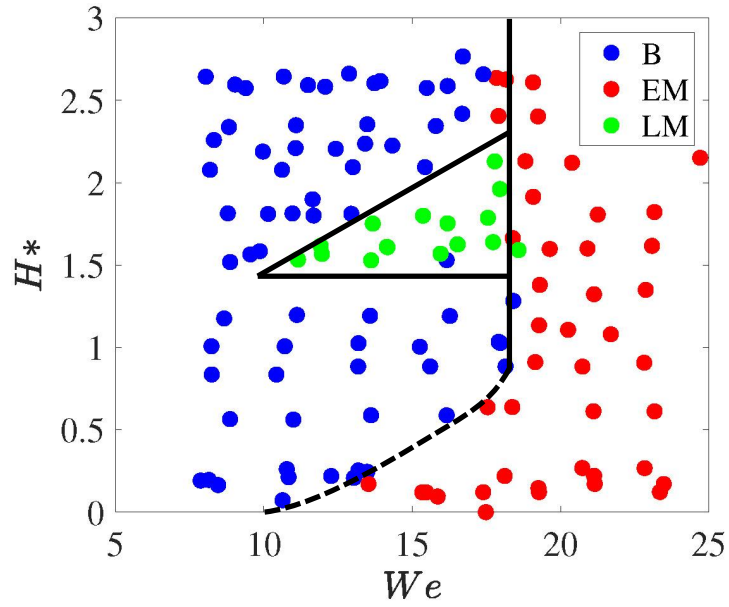
(a)
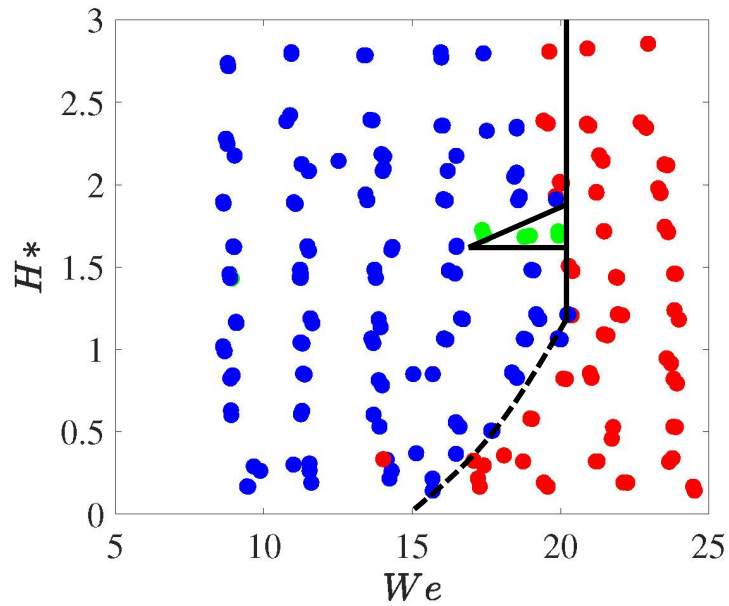
(b)

Figure 3.2: The regime graph of droplet impact outcomes in single-liquid systems for (a) S3 and (b) S4.5. Three different impact outcomes are shown in the figure: bouncing in blue, early merging in rad and late merging in green.

surface until the maximum penetration depth is reached at $t = 8$ ms. Here, the H^* is large enough to ensure that the penetration of the droplet would not be limited by the thickness of the film. Accordingly, after reaching the maximum penetration depth, the droplet starts to rebound (*bouncing*) using the surface energy stored during the penetration process. At a comparable H^* for a larger We, before the droplet reaches the maximum penetration depth for a given We, it merges with the film at $t = 2$ ms (*early merging*, fig 3.1.b).

When the H^* is lower for a sufficiently large We that ensures that the droplet penetrates to the physical limit of the pool, the droplet continues to spread horizontally along the solid surface of the chamber (both figure c and d) after it reaches the bottom of the pool. For a different We, the impact result varies between *bouncing* and *late merging*. Here at lower We the droplet bounces while the liquid film retracts (figure 3.1.c). However, at larger We the droplet merges in this retracting stage (*late merging*, figure 3.1.d).

Here, a regime graph is used to summarize the impact result with We and H^*, as shown in figure 3.2. Similar results for outcomes of droplet impact in single-liquid systems has been reported previously. The initial boundary is the vertical boundary demarcating the regime of *bouncing* and the regime of *early merging*. This boundary is independent of H^*. Both the deformation transition limit and the deep pool limit are boundaries which separate the *bouncing* and *late merging*. The deformation transition limit is independent of We(shown as a horizontal boundary in the regime graph). However, the deep pool limit is a function of both We and H^*. Here, the critical values for each transition limits vary with the type of the liquids used for

the experiment. We will next discuss and analyze this variability by performing a scaling analysis.

This regime graph for droplet impact on liquid films has been well established for single-liquid systems. For lower We, the impact does not result in breakage of the droplet or the air layer between the droplet and the film. This results in the *bouncing* of the droplet. However, when the We is large enough, the droplet breaks upon impacting the liquid film. This is known as *early merging*. Meanwhile, if the film thickness is smaller than the ideal maximum penetrating depth of drop, the film tends to prevent further penetration once the droplet reaches the bottom of the pool and instead spreads horizontally along the bottom surface of the chamber. Once the the droplet starts to retract after reaching the maximum spread position, if the film retracts faster than the droplet because of a much larger deformation in film the droplet merges with the film. This phenomena is known as *late merging*.

3.1.2 Two-liquid System

In the case of a two-liquid system, the impact outcomes for the droplet impact on a liquid film is affected by the liquid properties of both the droplet and the film. In experiments, we observed that the two-liquid system shows a richer regime diagram for impact outcomes compared to that for a single-liquid system. Further, with a change in the liquid combination in the two-liquid system, the transition limits that demarcates the different impact outcomes change.

Fig 3.3 shows the regime graph of the two-liquid system with liquid combinations. The transition boundaries in the regime diagram still exhibits similar behaviors that

21
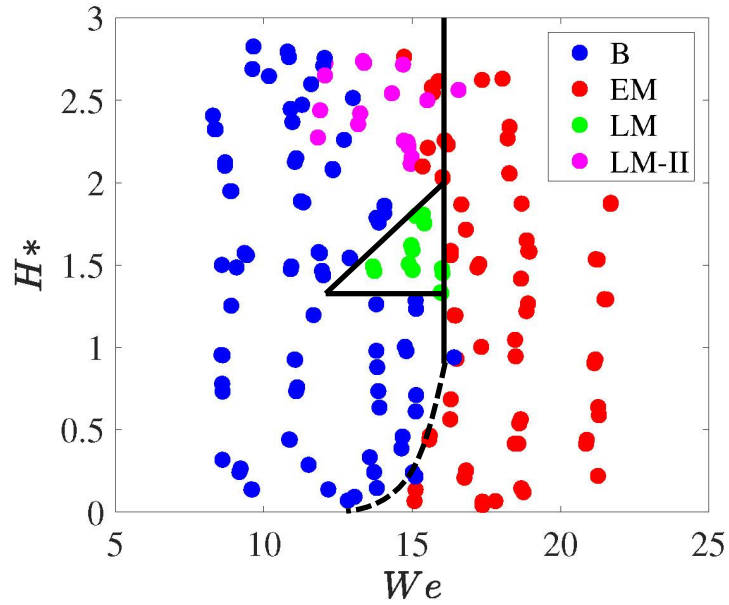
(a)
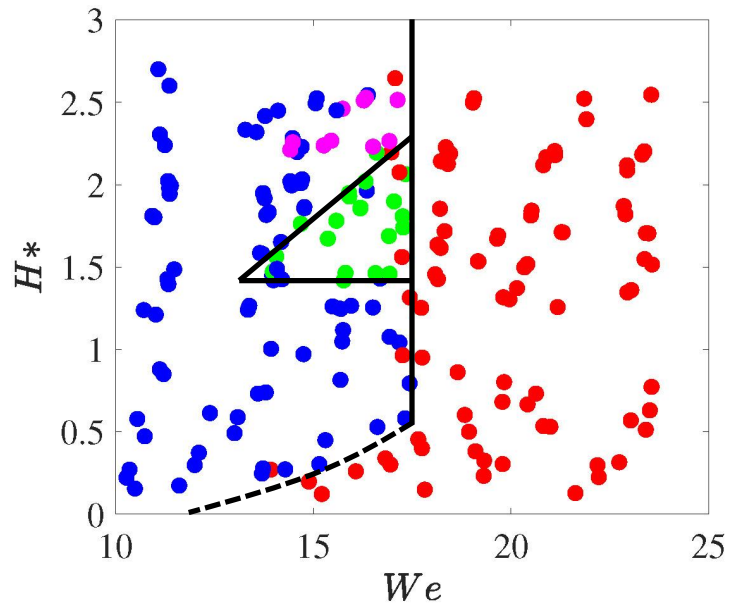
(b)

Figure 3.3: The regime graph of droplet impact outcomes in two-liquid systems for (a) S3 (droplet) to S4.5 (film) and (b) S4.5 to S3. Four different impact outcomes are shown : bouncing in blue, early merging in rad, late merging in green and late merging-II in pink.
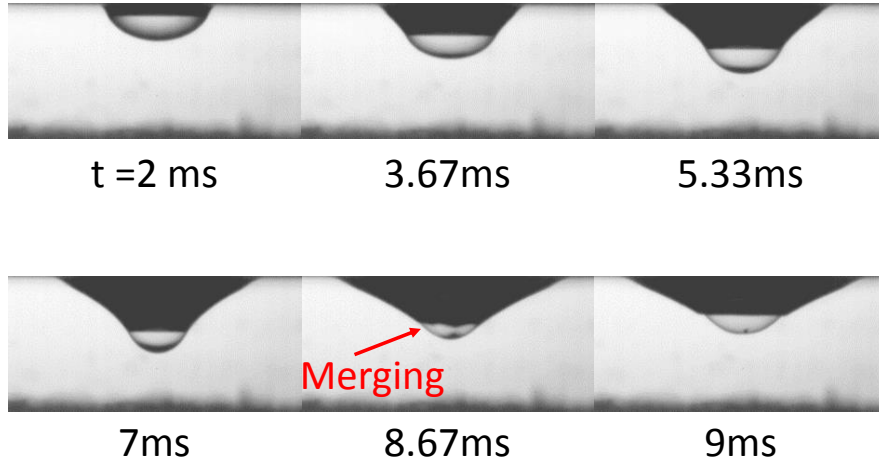
Figure 3.4: Side view observed in experiment in a two-liquid system about the late merging-II. Compared with bouncing case, the droplet merges with the film in the 'rebounding' process rather than finishing the rebounding process.

are observed in single-liquid system. However, for two-liquid systems, a new type of late merging not presented in single liquid systems was observed for high H^* (i.e. in a deep pool). we call this new type of merging in the two-liquid system as *Late merging-II*.

Fig 3.4 shows the side-view snapshots of the new type of impact outcome, *late merging-II*. Here both the We and H^* are not large enough for *early merging* nor for *late merging* to happen. During *late merging-II*, similar to the *bouncing* case in a deep pool, after reaching the maximum penetration depth, the droplet 'rebounds'. However, in between the process of rebounding, the droplet merges with the film at $t= 8.67$ ms .

3.2 Effect of Asymmetry in Liquid Properties

When the liquid properties of the droplet and the film are different, the impact outcomes are not only functions of We and $H*$, but also are influence by the ratio of liquid properties of the droplet and the film. Experimentally, we observe that the trends in shifting of the transition boundaries in the regime graph for two-liquid systems are not simple functions of liquid property ratios. In a single liquid system, the slope of the deep pool limit is always increasing with the viscosity. In contrast, in two-liquid system, the slope of the deep pool limit is not necessarily confined within the slopes of deep pool limits of the individual single-liquid systems. Since multiple liquid properties play a role in determining the outcome of impact, namely density, viscosity, and surface tension a complex non-linear relationship could be governing the impact outcomes in two-liquid systems. Thus, a scaling analysis is needed to explain this phenomena.

3.2.1 Inertial Limit

When a droplet impacts on a liquid film, before the potential merging happens or the droplet reaches the maximum penetration depth, the loss from the droplet's initial kinetic energy is converted to the kinetic energy, surface energy and viscous dissipation in both the droplet and the film. There would also be energy changes due to the gravity. However, considering that the the maximum penetration depth in the experiment is much smaller than the height from which the droplet starts accelerating towards the film, the effect of gravity can be ignored for simplicity.
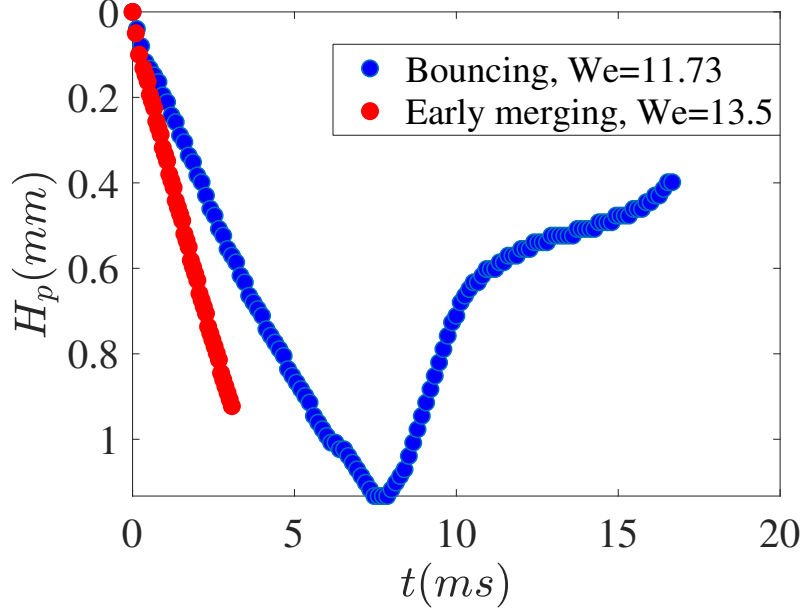
Figure 3.5: Penetration depth history in deep pool. Bouncing case is in blue while the early merging case is in red. Time t is from the last moment film remains undisturbed till the recorded time.

Moreover, considering that during the early stages of penetration droplet undergoes less deformation, the surface energy and the viscous dissipation in the droplet can also be ignored.

$$E_{kd,0} = E_{kd,p} + E_{kf,p} + (\Delta SE)_f + E_{\phi,f} \tag{3.1}$$

Here, $E_{kd,0}$ is the initial kinetic energy of the droplet. $E_{kd,p}$ and $E_{kf,p}$ are the kinetic energy of the droplet and film during the penetration. $(\Delta SE)_f$ and $E_{\phi,f}$ are the surface energy and viscous dissipation in the film.

As for the initial kinetic energy of the droplet $E_{kd,0}$ and the kinetic energy of

droplet during penetration $E_{kd,p}$,

$$E_{kd,0} = \frac{1}{2}\left(\rho_d \frac{4}{3}\pi R^3\right)U^2 = \frac{2}{3}\rho_d \pi R^3 U^2 \tag{3.2}$$

$$E_{kd,p} = \frac{1}{2}\left(\rho_d \frac{4}{3}\pi R^3\right)U_p^2 = \frac{2}{3}\rho_d \pi R^3 U_p^2 \tag{3.3}$$

From the penetration history obtained from experiments shown in figure 3.5, we can infer that the penetration velocity (slope from 0 to maximum penetration depth or merging position) is roughly constant during the process of penetration. Thus, here we assume that U_p remains as a constant during the penetration process.
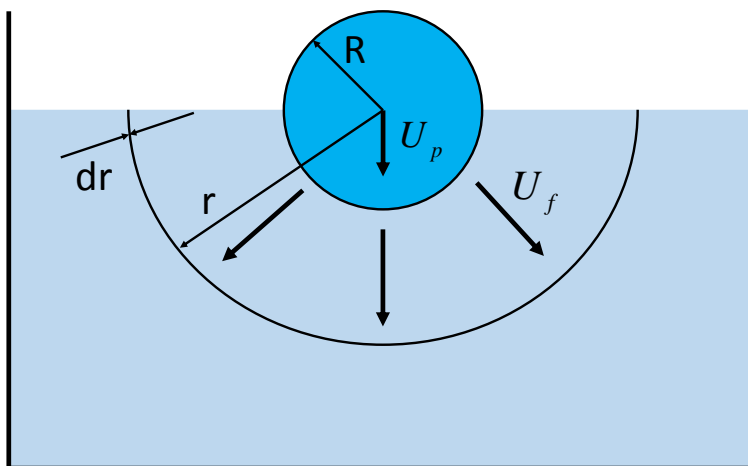
Figure 3.6: Schematic of the flow field in early penetration stage. The flow field in the film driven by the impact of droplet is modeled as a spherically symmetric radial flow. By integrating the flow field in the film, we can obtain the kinetic energy of the film.

26

To estimate the kinetic energy for the film in the early penetration stage, we can assume that the droplet introduces a spherically symmetric radial flow field in the film (figure 3.6), and the velocity scales as

$$U_f \approx U_P R^3 / r^3, \tag{3.4}$$

at the radial distance r from the center. By integrating the film's kinetic energy in a hemispherical shell of radius r and a thickness dr from $r = R$ to $r = \infty$, the kinetic energy in film can be obtained as:

$$E_{kf,p} = \int_R^\infty 2\pi \rho r^2 U_f^2 \mathrm{d}r \approx \int_R^\infty 2\pi \rho r^2 \left(U_{\mathrm{p}} R^3 / r^3 \right)^2 \mathrm{d}r = 2\pi \rho U_{\mathrm{p}}^2 R^3 \tag{3.5}$$

Here the induced velocity field is assumed to have a hemispherical symmetry with center of the hemisphere at the center of the droplet. When the droplet penetrates further inward into the pool, a simplified schematic of the penetration is considered as in fig 3.7, to estimate the surface energy and the viscus dissipation in the film. In a case where almost no horizontal spreading happens both in the droplet and the film, the horizontal velocity in the cylindrical surface shown in fig 3.7 is close to zero, so the contribution of kinetic energy of the film from the cylinder part can be ignored. Then, the surface energy change can be expressed as:

$$(\Delta SE)_f = \sigma_f \left[2\pi R \left(H_p - R \right) + 2\pi R^2 - \pi R^2 \right] = \sigma_f \pi R \left(2H_p - R \right) \tag{3.6}$$

Here the penetration depth (i.e., maximum penetration depth for the *bouncing*
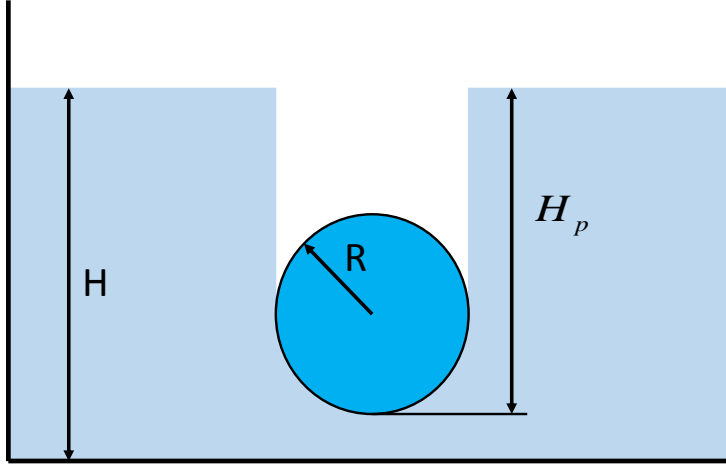
Figure 3.7: Schematic of non-spread penetration process in deep pool (before reach the maximum penetration depth). This model applies to all the penetration process without the physical limit from the film thickness.

case and merging depth for the *merging* case) is shown as a function of We from experiment data.

For viscous dissipation, in general,

$$E_\phi = \int_0^V \int_0^t \phi \, dV \, dt \approx \phi V t \qquad (3.7)$$

As for the viscous dissipation in the film, it can be divided into two parts: the viscous dissipation along the cylindrical surface $E_{\phi f,1}$ and the viscous dissipation along the hemispherical bottom $E_{\phi f,2}$.

$$E_{\phi,f} = E_{\phi f,1} + E_{\phi f,2} \qquad (3.8)$$

28

The contribution to viscous dissipation rate by the cylindrical surface in cylindrical polar coordinates (we neglect the rotational change),

$$\phi_f = \mu_f \left\{ 2 \left[\left(\frac{\partial u_r}{\partial r} \right)^2 + \left(\frac{u_r}{r} \right)^2 + \left(\frac{\partial u_z}{\partial z} \right)^2 \right] + \left[\frac{\partial u_r}{\partial z} + \frac{\partial u_z}{\partial r} \right]^2 \right\} \qquad (3.9)$$

For the cylindrical surface, assuming that the horizontal flow is not a function of z,

$$\frac{\partial u_r}{\partial z} \sim 0 \qquad (3.10)$$

We also assume there is no flow in the z direction along the cylindrical surface,

$$\frac{\partial u_z}{\partial r} \sim 0 \qquad (3.11)$$

Then $\frac{\partial u_z}{\partial r}$ can be obtained as the vertical velocity change across the boundary layer thickness δ, which is

$$\frac{\partial u_z}{\partial z} \sim \frac{U_p}{\delta} \qquad (3.12)$$

, from continuity

$$\frac{\partial u_r}{\partial r} + \frac{u_r}{r} \sim -\frac{\partial u_z}{\partial z} \sim -\frac{U_p}{\delta} \qquad (3.13)$$

As for the boundary layer thickness δ, here we assume (with t_m is the merging time from the impact moment till the merging happens):

$$\delta = \sqrt{\nu t_m} \qquad (3.14)$$

Considering there is no spread in horizontal direction where $\frac{u_r}{r} \sim 0$, then we have

$\frac{\partial u_r}{\partial r} \sim -\frac{U_p}{\delta}$.

Accordingly, the viscous dissipation rate in the cylinder surface of the film can be obtained as

$$\phi_f = 4\mu_f \left(\frac{U_P}{\delta}\right)^2 \tag{3.15}$$

For the viscous dissipation of the cylinder side surface in the film, the according merging time scale t_m is related with We from experimental data. Then the according viscous dissipation can be calculated as:

$$E_{\phi f,1} = \left(4\mu_f \left(\frac{U_P}{\delta}\right)^2\right) (2\pi R \left(H_p - R\right) \delta) t_m \tag{3.16}$$

The contribution for the viscous dissipation rate by the hemisphere surface in spherical coordinates,

$$\phi_f = 2\mu_f \left[\left(\frac{\partial u_r}{\partial r}\right)^2 + 2\left(\frac{u_r}{r}\right)^2\right] \tag{3.17}$$

Unlike the case in the cylindrical surface, here $\frac{\partial u_r}{\partial r} \sim -\frac{U_p}{\delta}$ and $\frac{u_r}{r} \sim \frac{U_p}{\delta}$.

Thus, the viscous dissipation rate of the bottom surface along the semi-sphere in the film is:

$$\phi_f = 6\mu_f \left(\frac{U_P}{\delta}\right)^2 \tag{3.18}$$

For the viscous dissipation in the film along the hemisphere surface, the according merging time scale t_m is proved as a function of We from experimental data. Then the according viscous dissipation can be calculated as:

$$E_{\phi f,2} = \left(6\mu_f \left(\frac{U_P}{\delta}\right)^2\right) \left(\pi R^2 \delta\right) t_m \tag{3.19}$$

After simplification, the penetration velocity can be expressed as:

$$U_p = \sqrt{\frac{\rho_d R^2 U^2 - 3\sigma_f(2H_p - R)}{\rho_d R^2 + 3\rho_f R^2 + 3\rho_f(4H_p - R)\sqrt{v_f t_m}}} \qquad (3.20)$$
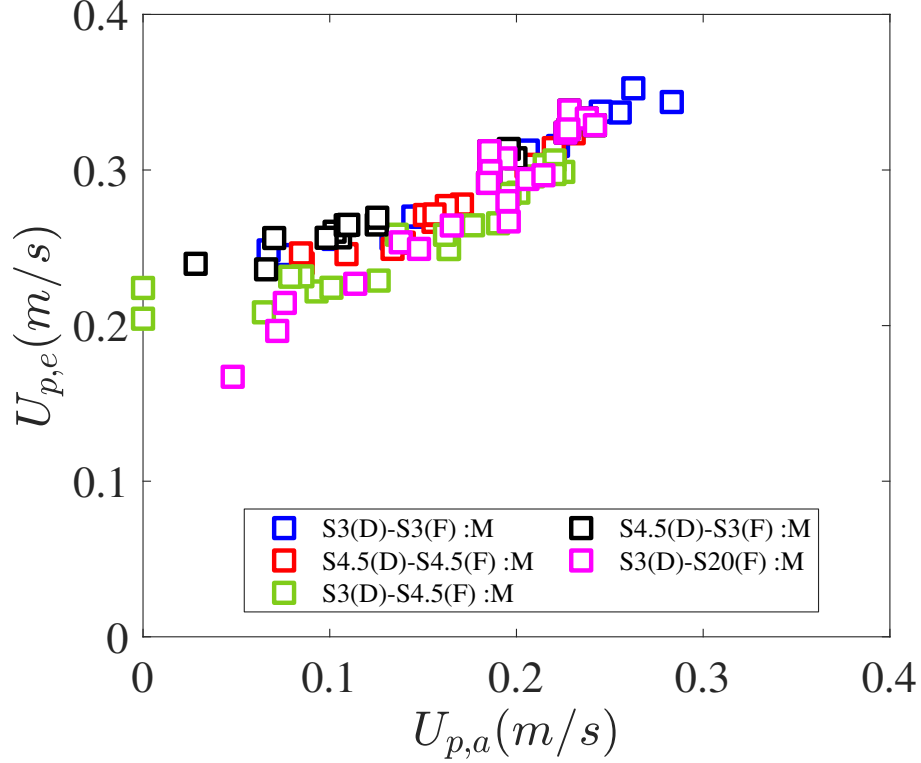
Figure 3.8: Penetration velocity calculated from both analysis and experiment. $U_{p,a}$ is the analytical penetration velocity calculated from eq 3.20. $U_{p,e}$ is the experimental penetration velocity calculated from eq 3.21

Here by applying the impact velocity, merging depth and merging time from individual experiments in eq 3.20, we can calculate the analytical penetration velocity $U_{p,a}$. Moreover, in the experiments, by assuming constant velocity of penetration for the droplet, the penetration velocity $U_{p,e}$ can be calculated as the average velocity

Table 3.1: Minimum averaged penetration velocity

Liquid	C10	C14	C10-C14	C14-C10	S3	S4.5	S3-S4.5	S4.5-S3
$U_p(m/s)$	0.301	0.278	0.202	0.241	0.245	0.240	0.204	0.236

taken to traverse the penetration depth (merging depth) for the duration of the penetration time (merging time):

$$U_{p,e} \approx \overline{U_p} = \frac{H_p}{t_m} \tag{3.21}$$

From figure 3.8, the analytical penetration velocity is compared with the experimental penetration velocity (average). Here these two penetration velocities have a linear relation, which means this scaling analysis fits well with the *early merging* conditions. However, the condition for the *early merging* to occur is determined by a critical minimum penetration velocity, which is different for different droplet and film liquid combinations (according to table 3.1). We hypothesis that this critical condition is related with the dynamics of the gas layer between the droplet and the film surface. Further study is needed to find this dependence of the critical penetration velocity on the liquid proprieties and it is out of the scope of the present thesis.

3.2.2 Deformation Transition Limit

As shown in the former study, the deformation transition limit is the limit where the impact outcome changes from *bouncing* to *late merging* in the same impact We with the an increase in the film thickness. The reason for this different impact

outcomes is the relative velocity of the film and the droplet during the rebounding stage. If the film returns faster than the droplet in the rebounding stage, the local pressure in the air layer would be higher leading to *late merging* of droplet with film. In another words, if the droplet moves faster than the film, the impact will end up as *bouncing*. Experimentally, we have investigated the penetration and breaking process corresponding to *late merging*, which is shown in figure 3.9a. From the energy balance in the rebounding stage, the kinetic energy in the droplet and the film is mainly derived from the surface energy of both droplet and film during the condition of the largest spreading. So the surface energy ratio can indirectly indicate the velocity difference between the droplet and the film during the rebound stage.

For the rebound stage, there exist a critical velocity ratio U_{crit}^* between the droplet rebounding velocity u_d and the film rebounding velocity u_f.

$$U^* = \frac{u_f}{u_d} \tag{3.22}$$

When the actual velocity ratio U^* is smaller the critical ratio, the droplet rebounds faster than the film, which will lead to *bouncing*. However, when the actual velocity ratio is larger than the critical ratio, the film will rebound faster than the droplet. This will decrease the gas layer thickness in-between and increase the local pressure, which will lead to *late merging*.

By assuming same volume scale V for droplet and film, the velocity ratio U^* can be expressed as a function of the kinetic energy ($E_{k,d}$ and $E_{k,f}$) and density of both
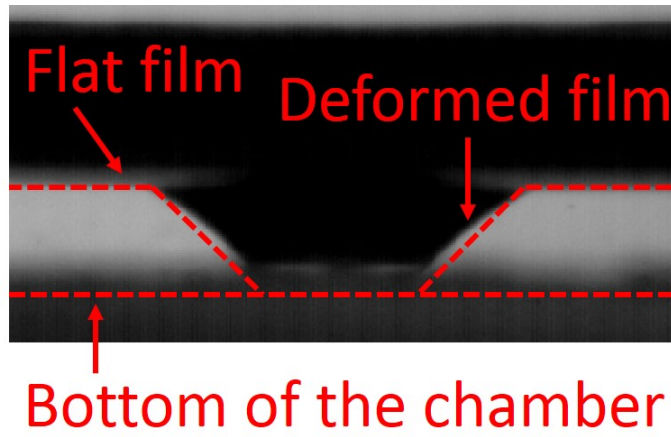
(a)
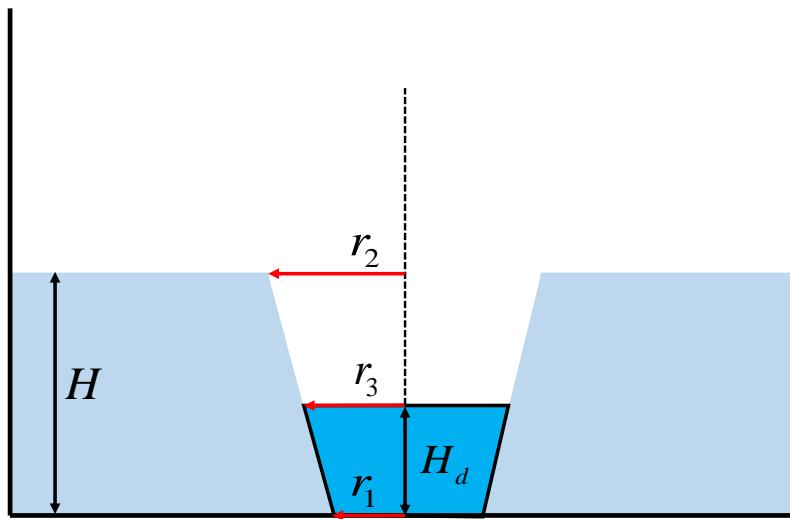
(b)

Figure 3.9: (a)Side view from the droplet impact experiment where the film spreads till the maximum deformation. (b)Schematic of the maximum spread deformation, with the droplet's and the film's maximum spread deformation as round table.

droplet and film:

$$U^* = \frac{u_f}{u_d} = \sqrt{\frac{u_f^2}{u_d^2}} = \sqrt{\frac{\frac{1}{\rho_f}\rho_f u_f^2 V}{\frac{1}{\rho_d}\rho_d u_d^2 V}} = \sqrt{\frac{\frac{1}{\rho_f}E_{k,f}}{\frac{1}{\rho_d}E_{k,d}}} \tag{3.23}$$

During the rebounding stage, the kinetic energy in either the droplet or the film is mainly derived from its own surface energy. Thus, less energy is transferred between the droplet and the film. Therefore, kinetic energy can be expressed by surface energy $((\Delta SE)_d$ and $(\Delta SE)_f)$ and viscous dissipation $(\phi_d$ and $\phi_f)$ from energy equilibrium for both droplet and film

$$E_{k,d} = (\Delta SE)_d - E_{\phi,d} \tag{3.24}$$

$$E_{k,f} = (\Delta SE)_f - E_{\phi,f} \tag{3.25}$$

Experimentally, the surface area in the droplet and the film can be calculated by the side view at the condition of maximum spreading. Here for the actual deformation, assume a round table shape for both the droplet and the film as shown in figure 3.9b. As for the film, the bottom radius r_1 and the top radius r_2 can be expressed according to the spread ratio $(w_1^*$ and $w_2^*)$ and the initial radius of droplet:

$$r_{1,f} = w_1^* R \tag{3.26}$$

$$r_{2,f} = w_2^* R \tag{3.27}$$

Thus the surface area difference ΔA_f in the film between surface area at the

initial stage $A_{0,f}$ and surface area at the maximum spread $A_{\max,f}$ can be calculated as:

$$
\begin{aligned}
\Delta A_f &= A_{\max,f} - A_{0,f} \\
&= \pi \left[r_1^2 + r_2^2 + (r_1 + r_2) \sqrt{H^2 + (r_2 - r_1)^2} \right] - \pi r_2^2 \\
&= \pi \left[r_1^2 + (r_1 + r_2) \sqrt{H^2 + (r_2 - r_1)^2} \right] \\
&= \pi R^2 \left[w_1^{*2} + (w_1^* + w_2^*) \sqrt{H^{*2} + (w_2^* - w_1^*)^2} \right]
\end{aligned}
\tag{3.28}
$$

As for the droplet, since it is hard to measure the droplet shape from the experiment, here we assume a similar round table shape for droplet. Here the droplet shares the same bottom radius r_1 as that of the film. With an unknown top radius r_3 and the height H_d, the surface area difference in droplet ΔA_d (between surface area at the initial stage $A_{0,d}$ and surface area at the maximum spread $A_{\max,d}$) can be expressed as:

$$
\begin{aligned}
\Delta A_d &= A_{\max,d} - A_{0,d} \\
&= \pi \left[r_1^2 + r_3^2 + (r_1 + r_3) \sqrt{H_d^2 + (r_3 - r_1)^2} \right] - 4\pi R^2 \\
&= \pi R^2 \left[w_1^{*2} + w_3^{*2} - 4 + (w_1^* + w_3^*) \sqrt{H_d^{*2} + (w_3^* - w_1^*)^2} \right]
\end{aligned}
\tag{3.29}
$$

However, these two unknowns can be expressed by r_1, r_2 and H from volume conservation and geometric similarity:

$$
\frac{\pi H_d}{3} \left(r_3^2 + r_1^2 + r_3 r_1 \right) = \frac{4}{3} \pi R^3
\tag{3.30}
$$

$$
\frac{r_3 - r_1}{H_d} = \frac{r_2 - r_1}{H}
\tag{3.31}
$$

36

Then, we get the expression of both r_3 and H_d:

$$r_3 = \left(r_1^3 + 4R^3\frac{r_2 - r_1}{H}\right)^{\frac{1}{3}} \tag{3.32}$$

$$H_d = \frac{H}{r_2 - r_1}\left[\left(r_1^3 + 4R^3\frac{r_2 - r_1}{H}\right)^{\frac{1}{3}} - r_1\right] \tag{3.33}$$

Thus experimentally both the surface area difference in droplet and film can be calculated. From figure 3.10 a and b, both the spread ratio in top and bottom exhibits large variance. For different liquid combination, the ratio of the surface area difference in droplet and film ΔA^* collapse into a second order equation with the dimensionless film thickness H^*.

$$\Delta A^* = \frac{\Delta A_f}{\Delta A_d} \tag{3.34}$$

As for the viscous dissipation, from the maximum spreading to the merging point, it can be modeled as $E_\phi = E_0\left(1 - e^{-2\eta\Delta t}\right)$. Here E_0 is the initial energy, which is the surface energy of the droplet or film when the retracting starts. Δt is the elapsed time from the maximum spread to the merging point. Also, we have $\eta = \frac{8\nu}{R}$. The time scale related to this is the capillary time scale $\Delta t \approx t_{\text{cap}} = C_{\text{cap}}\left(\rho R^3/\sigma\right)^{1/2}$, where C_{cap} is a proportionality constant. From experiment data, C_{cap} varies between 0.1 to 1. Here in the following calculation, C_{cap} is used as 1.

Thus, it can be modeled as:

$$E_{\phi,d} = E_{0,d}\left(1 - e^{-2\eta_d\Delta t}\right) = (\Delta SE)_d\left(1 - e^{-2C_{cap}Oh_d}\right) \tag{3.35}$$
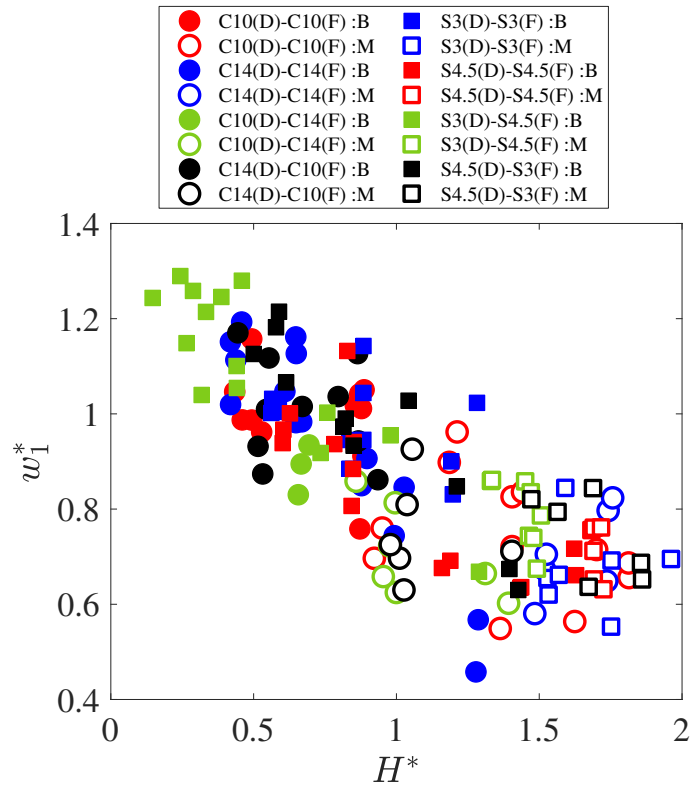
(a)
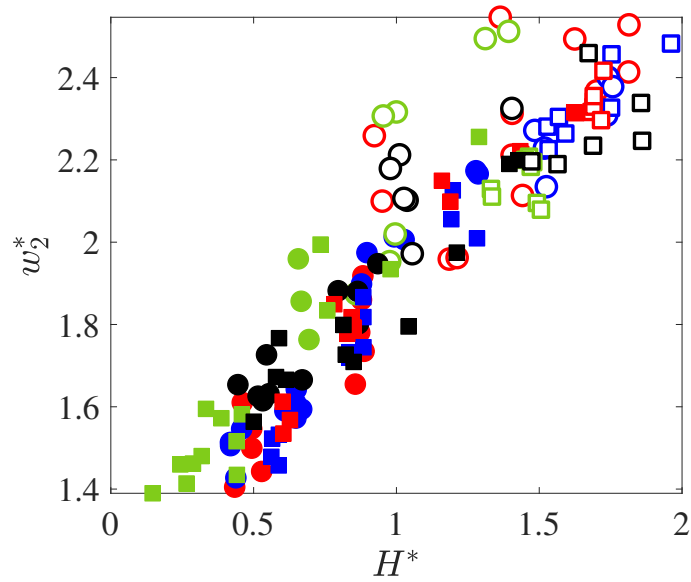
(b)

Figure 3.10: (a)w_1^* as a function of H^*. (b)w_2^* as a function of H^*. Here both the spread ration have large variance.

38
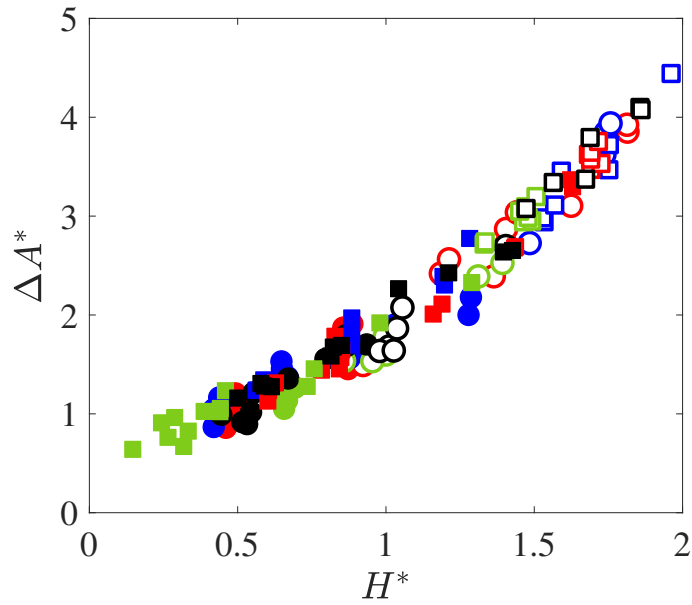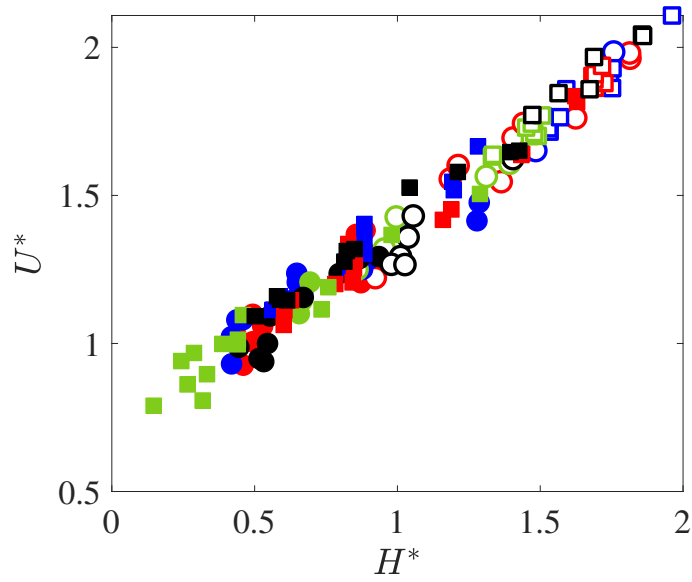
Figure 3.11: (a)Area ratio ΔA^* as a function of H^*. The ratio of the surface area collapse into a second order equation with the film thickness.(b)Rebounding velocity ratio U^* calculated from eq 3.33 as a function of H^*. This figure shears same legend as figure 3.10

39

Table 3.2: Critical rebounding velocity ratio

Liquid	C10	C14	C10-C14	C14-C10	S3	S4.5	S3-S4.5	S4.5-S3
U^*_{crit}	1.382	1.476	1.207	1.327	1.666	1.835	1.505	1.651

$$E_{\phi,f} = E_{0,f}\left(1 - e^{-2\eta_f \Delta t}\right) = (\Delta SE)_f \left(1 - e^{-2C_{cap}Oh_f}\right) \tag{3.36}$$

Therefor, the energy equilibrium equations can be simplified with the velocity ratio U^* as:

$$U^* = \sqrt{\left(\frac{\rho_d}{\rho_f}\right)\left(\frac{\sigma_f}{\sigma_d}\right)\left(\frac{e^{-2C_{cap}Oh_f}}{e^{-2C_{cap}Oh_d}}\right)\Delta A^*} \tag{3.37}$$

However, in the spreading process, the area ratio is mainly controlled by the film thickness, which we can see from figure 3.11.a. Accordingly, the velocity ratio also depends on the film thickness. We observe from the dependence of the velocity ratio on film thickness (shown in the figure 3.11.b) that the liquid ratios of proprieties' have weaker influence on the velocity ratio than the film thickness. All of the velocity ratios collapse into one single line, in most of the experimental data (figure 3.11.b). However, the critical velocity ratio condition that determines the deformation transition limit remains unknown. It is clear that the critical velocity ratio is related to both the droplet's and the film's liquid proprieties, since it varies in a large range for different liquid combinations as can be observed in table 3.2.

Further study is needed to explain the retracting process and the dependence of the critical velocity ratio that determines the deformation transition limits for outcome of droplet impact on liquid film.

3.2.3 Deep Pool Limit

As discussed above, while increasing the film thickness maintaining a rather low We, a second type of merging - *late merging* is observed. If we increase film thickness from this point, through deep pool limit, the *late merging* transfers to *bouncing*. Physically, it shows that the impact We is less than the critical value which can support the drop to reach the bottom of the liquid film. From the experiment, the penetration depth history is recorded using image processing, as shown in fig 3.12. As we can see, with the We increasing, the maximum penetration depth H_{pm} is also increasing. To compare the influence of the We and the liquid proprieties on the maximum penetration depth, the maximum penetration depth is recorded, this is shown in figure 3.13.

However, the similar to the other two transition limits, the slope of the deep pool limit for a two-liquid system is not confined within in the range of slopes for the deep pool limits of single-liquid systems consisting of the individual liquids that constitutes the two-liquid system. Take the Alkane group for example, from fig 3.13, the dimensionless maximum penetration depth $(H_{pm}^* = H_{pm}/R)$ for C10-C14 group is lower than the penetration depth for single-liquid systems consisting of C10 or C14. However, if we were to switch the liquids in the droplet and the film, the penetration depth in C14-C10 groups are very close to the penetration depth for the single-liquid system. Furthermore, in the case of silicone oil, the two-liquid system penetration depth curves (S3-S4.5 and S4.5-S3) are in between the single-liquid system curves (S3 and S4.5). It is because viscus dissipation plays an important role in determining this penetration process. This makes this process a highly nonlinear. Thus we use a
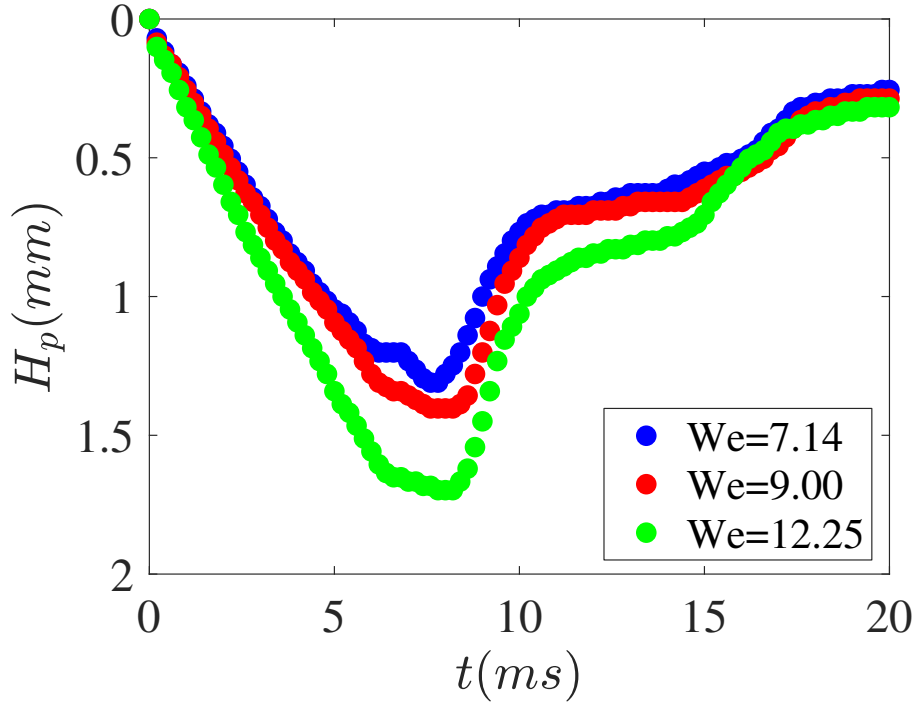
Figure 3.12: Penetration depth history with different Weber number in deep pool. With the increasing of the Weber number, in another words, with more initial kinetic energy of the droplet, the film is deformed till a deeper penetration depth.

analysis is to explain this phenomena.

When a droplet impacts a liquid film, until the maximum penetration is achieved, the loss from the droplet's initial kinetic energy is converting to the kinetic energy, surface energy and viscous dissipation in the droplet and the film. There would also be energy changes due to gravity. Considering that the the maximum penetration depth in the experiment is much smaller than the height from which the droplet starts accelerating towards the film, the effect of gravity can be ignored for simplicity.

$$E_{kd,0} = (\Delta SE)_f + (\Delta SE)_d + E_{\phi,d} + E_{\phi,f} \tag{3.38}$$
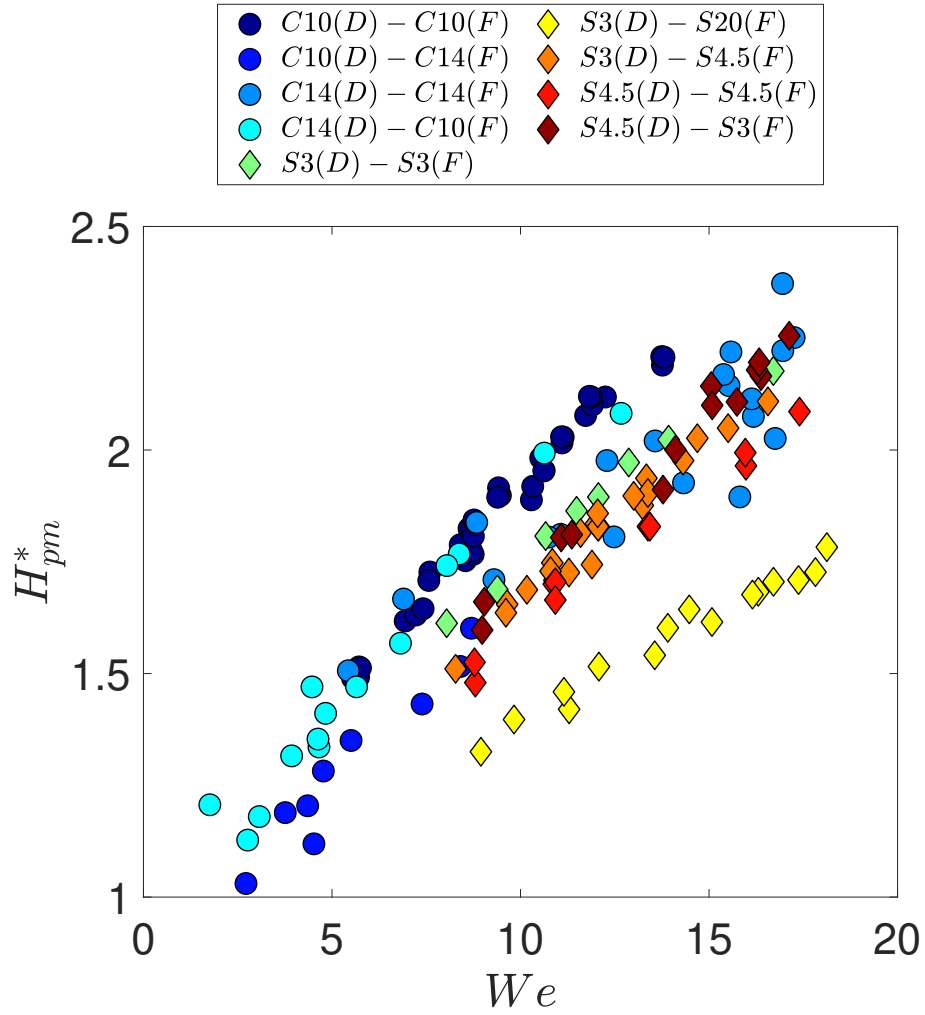
Figure 3.13: Dimensionless maximum penetration depth varies with Weber number. The dimensionless maximum penetration depth H_{pm}^* in each individual experiment is recorded and plotted with the droplet Weber number.

As for the initial kinetic energy of droplet,

$$E_{kd,0} = \frac{1}{2}\left(\rho_d \frac{4}{3}\pi R^3\right)U^2 = \frac{2}{3}\rho_d \pi R^3 U^2 \tag{3.39}$$
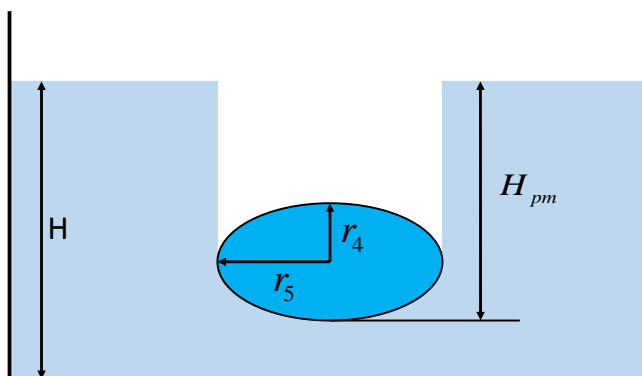
Figure 3.14: Schematic of the maximum penetration depth. As the film has the maximum deformation in the penetration process, the tip of the film reaches the maximum penetration depth. Here, the horizontal spread is considered using the spread ratio $w_5^* = \frac{r_5}{R}$.

While the droplet impacts on the liquid film and reaches the maximum penetration depth, without any restrictions from the physical limit dictated by the film thickness, the initial kinetic energy of the droplet is converted into surface tension and the viscous dissipation both in droplet and the film. To simplify the model, we assume a cylindrical deformation in the film with a penetration depth H_{pm} and a semi-ellipsoid surface at the bottom with major axis equal to r_5. As for the droplet, an ellipsoid deformation is assumed with the horizontal radius r_5 and vertical radius r_4, as shown in figure 3.14. Then the surface energy change can be expressed

with $w_5^* = \frac{r_5}{R}$ and $r_{45}^* = \frac{r_4}{r_5} = w_5^{*-3}$ (from the mass conservation), considering less horizontal spread ($w_5^* \approx 1$):

$$(\Delta SE)_f = \sigma_f \left[2\pi R w_5^* (H_{pm} - R) + 2\pi R^2 - \pi R^2 \right] = \sigma_f \pi R (2H_{pm} - R) \qquad (3.40)$$

$$
\begin{aligned}
(\Delta SE)_d &= \sigma_d \left(A_e - 4\pi R^2 \right) \\
&= \sigma_d \left[2\pi r_5^2 \left(1 + \frac{r_4^2}{\sqrt{1-r_{45}^{*2}r_5^2}} \tanh^{-1}(\sqrt{1-r_{45}^{*2}}) \right) - 4\pi R^2 \right] \\
&= \sigma_d \pi R^2 \left[2w_5^{*2} \left(1 + \frac{r_{45}^{*2}}{\sqrt{1-r_{45}^{*2}}} \frac{1}{2} \ln \left(\frac{1+\sqrt{1-r_{45}^{*2}}}{1-\sqrt{1-r_{45}^{*2}}} \right) \right) - 4 \right] \\
&= \sigma_d \pi R^2 \left[2w_5^{*2} \left(1 + \frac{w_5^{*-6}}{\sqrt{1-w_5^{*-6}}} \frac{1}{2} \ln \left(\frac{1+\sqrt{1-w_5^{*-6}}}{1-\sqrt{1-w_5^{*-6}}} \right) \right) - 4 \right]
\end{aligned}
\qquad (3.41)
$$

However, with small droplet deformation, in another words, when $w_5^* \approx 1$, the surface energy change in droplet can be ignored.

Accordingly, the viscous dissipation rate in the cylinder's side surface of the film can be obtained as

$$\phi_f = 4\mu_f \left(\frac{U_P}{\delta} \right)^2 \qquad (3.42)$$

For the viscous dissipation of the cylinder's side surface in the film, assume the capillary penetration time scale $t_{cap} = 2\pi \sqrt{\frac{\rho_d R^3}{8\sigma_d}}$, and the boundary layer thickness $\delta = \sqrt{v_f t_{cap}}$. Then the viscous dissipation in the film along the cylinder's side surface can be calculated as:

$$E_{\phi f, 1} \approx \left(4\mu_f \left(\frac{U_P}{\delta} \right)^2 \right) (2\pi R (H_{pm} - R) \delta) t_{cap} \qquad (3.43)$$

As for the viscous dissipation rate of the hemisphere surface in spherical coordi-

nates,

$$\phi_f = 6\mu_f \left(\frac{U_P}{\delta}\right)^2 \tag{3.44}$$

The viscous dissipation in the film along the hemisphere surface can be calculated as:

$$E_{\phi f,2} \approx \left(6\mu_f \left(\frac{U_P}{\delta}\right)^2\right)\left(\pi R^2 \delta\right) t_m \tag{3.45}$$

The viscous dissipation rate in the droplet, in the 3-D Cartesian coordinate system is given as,

$$\phi_d = 2\mu_d \left[\left(\frac{\partial u_x}{\partial x}\right)^2 + \left(\frac{\partial u_y}{\partial y}\right)^2 + \left(\frac{\partial u_z}{\partial z}\right)^2\right]$$

$$+ \mu_d \left[\left(\frac{\partial u_x}{\partial y} + \frac{\partial u_y}{\partial x}\right)^2 + \left(\frac{\partial u_x}{\partial z} + \frac{\partial u_z}{\partial x}\right)^2 + \left(\frac{\partial u_y}{\partial z} + \frac{\partial u_z}{\partial y}\right)^2\right] \tag{3.46}$$

$\frac{\partial u_z}{\partial z}$ can be obtained as the vertical velocity change across the radius, which is $\frac{\partial u_z}{\partial z} \sim \frac{U_p}{R_0}$. To simplify, consider the droplet spreading from the center without any rotation, then we have $\frac{\partial u_x}{\partial x} = \frac{\partial u_y}{\partial y} = \frac{\partial u_z}{\partial z} \sim \frac{U_p}{R_2}, \frac{\partial u_x}{\partial y} = \frac{\partial u_x}{\partial z} = \frac{\partial u_y}{\partial x} = \frac{\partial u_y}{\partial z} = \frac{\partial u_z}{\partial x} = \frac{\partial u_z}{\partial y} = 0$.

Accordingly, the viscous dissipation rate in droplet can be obtained as

$$\phi_d = 6\mu_d \left(\frac{U_P}{r_5}\right)^2 \tag{3.47}$$

The viscous dissipation in the droplet, using the volume of droplet and the same

capillary penetration time scale t_{cap} can be expressed as:

$$E_{\phi,d} \approx \left(6\mu_d \left(\frac{U_P}{r_5}\right)^2\right)\left(\frac{4}{3}\pi R^3\right) t_{cap} \tag{3.48}$$

However, both in the film and the droplet viscous dissipation scaling, the velocity used is only the penetration velocity rather than the impact velocity. Thus the relation between these two velocity are needed. From the penetration history figure we can tell that the penetration velocity Up is reduced from the impact velocity U, and is remaining almost a constant in the whole penetration process. So the penetration velocity from the early penetration stage can be taken as the average penetration velocity. However, in the early penetration stage, less effects from both surface deformation and viscous dissipation are applied. Thus for the energy equilibrium in the early penetration stage, the surface tension terms and the viscous dissipation terms can be ignored:

$$E_{kd,0} = E_{kf,p} + E_{kd,p} \tag{3.49}$$

In order to estimate the kinetic energy in the early penetration stage, we can assume that the droplet induces a spherically symmetric radial flow field in the film, and the velocity scales as

$$V \approx U_P R^3 / r^3, \tag{3.50}$$

at the radial distance r from the center. By integrating the film kinetic energy from r with a thickness dr, the kinetic energy in film can be obtained as:

$$E_{kf,p} = \int_R^\infty 2\pi\rho r^2 U_f^2 \mathrm{d}r \approx \int_R^\infty 2\pi\rho r^2 \left(U_\mathrm{p}R^3/r^3\right)^2 \mathrm{d}r = 2\pi\rho U_\mathrm{p}^2 R^3 \tag{3.51}$$

47

As for the kinetic energy of droplet, since it is in early penetration stage, we ignore the deformation in the droplet:

$$E_{kd,p} = \frac{1}{2}\left(\rho_d \frac{4}{3}\pi R^3\right)U_p^2 = \frac{2}{3}\rho_d \pi R^3 U_p^2 \tag{3.52}$$

Moreover, by considering the energy equilibrium in the early penetration stage, the square ratio of the penetration velocity and the initial velocity can be expressed as a function of both droplet and film density:

$$\frac{U_p^2}{U^2} = \frac{1}{1+3\frac{\rho_f}{\rho_d}} \tag{3.53}$$

In the case when droplet and film liquids are the same, the square ratio will be 1/4, which has been proved in former study. Assuming this relation, the scale of penetration velocity will be controlled by the impact velocity, and densities of liquids that constitute the droplet and the film:

$$U_p = \sqrt{\frac{1}{1+3\frac{\rho_f}{\rho_d}}}U \tag{3.54}$$

By distinguishing each term in the energy balance, after simplification, the dimensionless parameter $H_{pm}^* = \frac{H_{pm}}{R}$ can be shown as:

$$H_{pm}^* =$$
$$\frac{\left[\frac{1}{6}\left(\frac{\sigma_d}{\sigma_f}\right)-2\pi\left(\frac{1}{1+3\frac{\rho_f}{\rho_d}}\right)\left(\frac{\sigma_d}{\sigma_f}\right)Oh_d-\frac{1}{2}\left(\frac{\pi}{2}\right)^{\frac{1}{2}}\left(\frac{1}{1+3\frac{\rho_f}{\rho_d}}\right)\left(\frac{\sigma_d}{\sigma_f}\right)\left(\frac{\rho_d}{\rho_f}\right)^{-1}\left(\frac{v_d}{v_f}\right)^{-\frac{1}{2}}Oh_d^{\frac{1}{2}}\right]We_d+\frac{1}{2}}{1+2\left(\frac{\pi}{2}\right)^{\frac{1}{2}}\left(\frac{1}{1+3\frac{\rho_f}{\rho_d}}\right)\left(\frac{\sigma_d}{\sigma_f}\right)\left(\frac{\rho_d}{\rho_f}\right)^{-1}\left(\frac{v_d}{v_f}\right)^{-\frac{1}{2}}Oh_d^{\frac{1}{2}}We_d} \tag{3.55}$$

48

Here, the droplet Ohnesorge number is defined as:

$$\mathrm{Oh_d} = \frac{\mu_d}{\sqrt{\rho_d \sigma_d (2R)}} \tag{3.56}$$

In the condition that there is no large deformation in the droplet, in another words, assuming $w_5^* \approx 1$, the surface energy term of droplet can be ignored. Then, the equation of dimensionless penetration depth collapses to an equation with several constant terms, different ratios of liquid properties, impact Weber number and droplet Ohnesorge number. From this simplified equation, we can infer that the dominant term that determines the the penetration depth is the initial kinetic energy term for droplet, which is essentially the source of the energy in the system. Also, in low viscous liquid, in another words, terms with low droplet Ohnesorge number have a weak effect on the penetration depth. However, compared with former studies on the penetration depth, the improvement in the agreement between the experimental maximum penetration depth $H_{pm,e}^*$ and the analytical maximum penetration depth $H_{pm,a}^*$ is quite clear (from figure 3.15). The maximum penetration depth is no longer simply a linear function of the impact Weber number, when we consider the viscus dissipation.

3.3 Late Merging-II

As mentioned previously during the discussion of outcomes of impact of droplet on a liquid film in a two-liquid system, there is a unique phenomena of *late merging-*
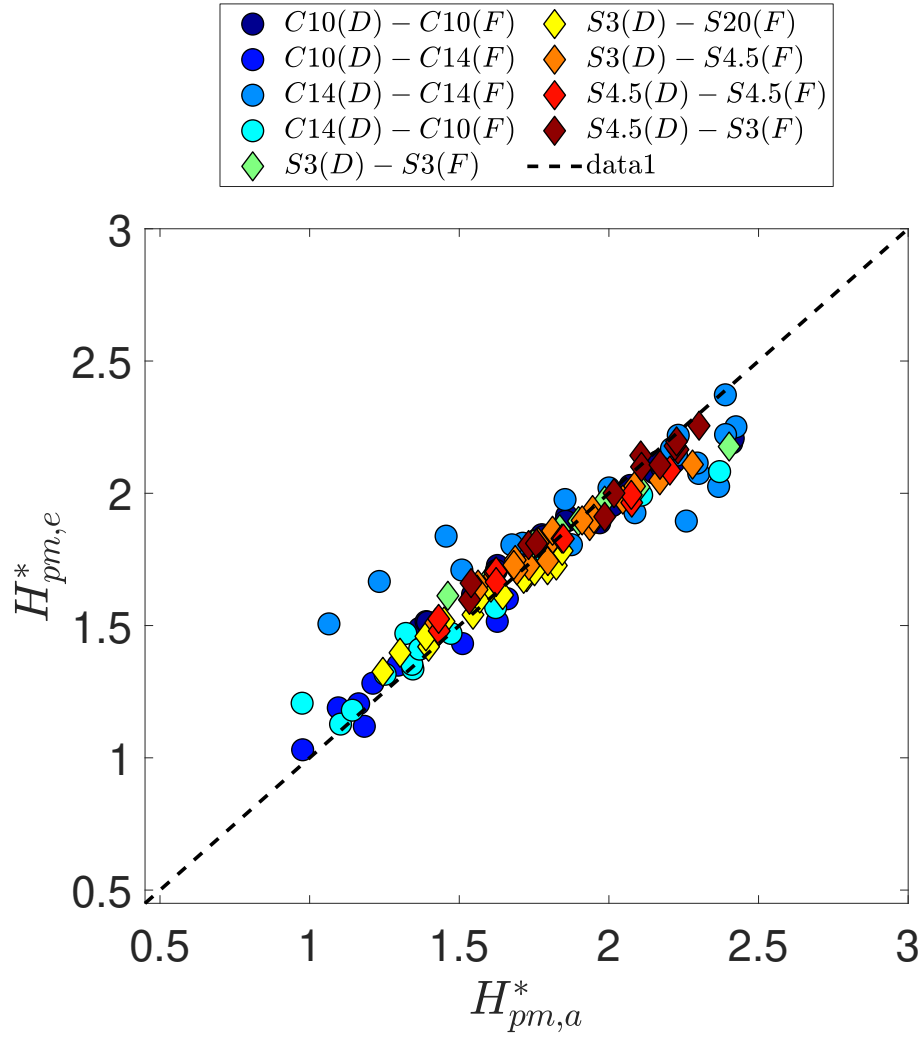
Figure 3.15: Maximum penetration depth from scaling analysis and experiment. The maximum penetration depth from experiment is recorded as shown in fig 3.13. The analytical maximum penetration depth is from eq 3.55.

t =8.2ms   8.67ms   9.53ms   10.2ms   10.87ms   11.53ms

(a) Bouncing in C10, We=8.4, H*=3

t =8.6ms   9.27ms   9.93ms   10ms   10.07ms   10.13ms

(b) Late merging II in C14-C10, We=8.37, H*=2.8

Figure 3.16: (a) The side view of bouncing outcome from droplet impact on a liquid film experiment in a single-liquid system. (b) The side view of late merging-II outcome from droplet impact on a liquid film experiment in a two-liquid system.

Table 3.3: Experiemt liquid capilliary time

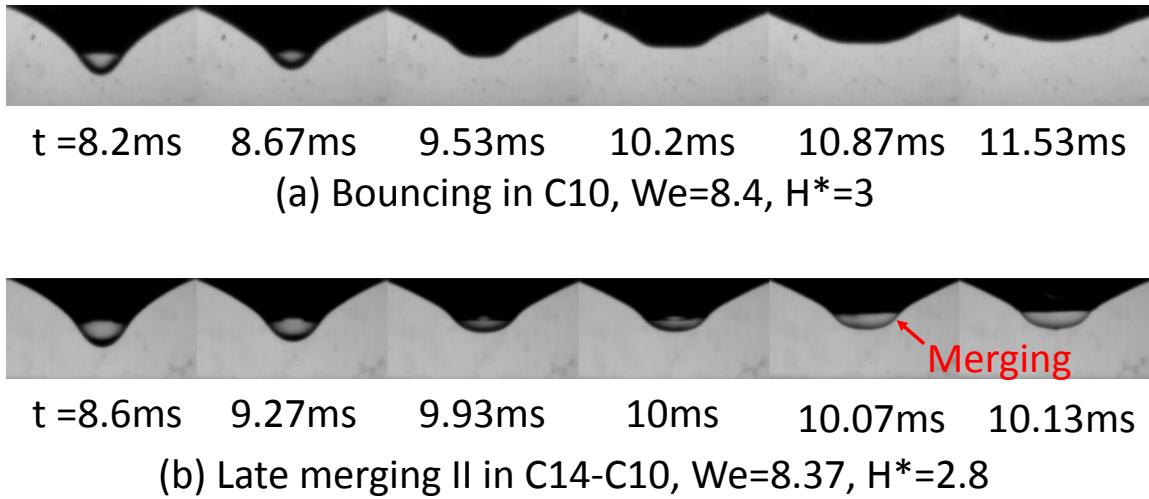| Liquid	Capillary Time(ms)
C10	8.804
C14	9.031
S3	9.540
S4.5	9.474
S20	8.965

II. As we can see from figure 3.16, in a single liquid system with low We and high H^*, droplet reaches the maximum penetration and rebound. However, in the two-liquid system, the droplet may merge during this the rebound process. From the figure 3.16.b, we can observe that the liquid film boundary becomes flatter quickly at the point of deepest depression.

As this type of merging always happen in the deep pool condition, this can not be due to the effect of finite film thickness. One of the remaining possible reasons for existence of *Late merging-II* in two-liquid system but not in one-liquid system, is difference in the propagation velocity of the capillary wave (and hence the capillary time scale) in the droplet and film due to difference in their liquid properties.

For the undamped frequency of the film as in the oscillating system, it is affected by both the liquid properities, the thickness of film and the wave number $k \approx 2/R$:

$$\omega_{\text{cap}} = \sqrt{(\sigma k^3/\rho)\tanh(kH)} \tag{3.57}$$

In the deep pool case, dimensionless film thickness H^* is much larger than 1. In another words, the $\tanh(kH)$ is close to 1. Thus the capillary time can be simplified

as:

$$t_{cap} = 2\pi\sqrt{\frac{\rho R^3}{8\sigma}} \tag{3.58}$$

Since the retraction process is enable via a capillary wave, in table 3.3 the capillary time in all the experiment liquids are compared. Here we can observe that there exists a phase difference between droplet and film surface caused by different liquid proprieties.

Chapter 4

Conclusions

This chapter summarizes the results both from experimental and theoretical studies presented in Chapter 2 and Chapter 3. Further, as an extension to this thesis, we identify a few interesting problems that could be pursued in future research endeavors.

4.1   Summary

The experiments were conducted for both single-liquid systems and two-liquid systems. Though the liquid propriety ratios are limited by the limited choice of liquids, four distinct types of impact outcomes are observed by changing the droplet impact velocity, film thickness and the liquid combination. The different outcomes of impact are a)*bouncing* of the droplet, b)*early merging* where the droplet merges with the film before it reaches maximum penetration depth, c) *late merging* where the droplet merges with the film during the retraction process after the droplet reaches

a maximum penetration depth as limited by the film thickness. Since the maximum penetration depth in this case is limited by the film thickness, as the droplet reaches the maximum penetration depth, it also spreads horizontally before it starts the process of retraction. The retraction process results in the restoration of kinetic energy of both film and the droplet through a reduction in their surface area, d) *late merging-II* where the droplet merges during the retraction process after the droplet reaches the maximum penetration depth not limited by the film thickness. Note that *late merging-II* only occurs for a limited impact condition and only for two-liquid systems.

We construct a regime diagram for droplet impact outcome by mapping the impact outcomes in $We - H^*$ plane. We see that there are 3 clear boundaries that separates the different regimes of impact outcomes. a) *inertial limit* that marks the boundary between the *bouncing* and the *early merging*, b) *deformation transition limit* marking the boundary between *bouncing* and *late merging* independent of We, c) *deep pool limit* marking the *bouncing* and *late merging* as a function of both H^* and We. Corresponding to each of these regime boundaries, we develop theoretical models that captures the scaling behavior of the underlying physical mechanism that drives the transition.

In the case of inertial limit, the penetration velocity is calculated both experimentally and analytically. From experiments and theoretical analysis, we observe that there exists a critical penetration velocity for a given droplet-film liquid combination, which is independent of film thickness, beyond which the droplet impact results in *early merging*. In comparison to the critical velocity for maximum trapped

bubble size for the droplet impact on a solid surface which does not depend up on the properties of the solid surface, the critical velocity corresponding to the inertial limit for a droplet impact on a film, depends on both the droplet and film liquid proprieties.

As for the deformation transition limit, the retracting velocity ratio decides the impact results. We calculate the retracting velocity ratio by identifying the geometry corresponding to the maximum spread of droplet in the shallow pool. Interestingly, the area ratio corresponding to the state of maximum spread is only a function of film thickness implying that the process of spreading is independent of the droplet impact velocity and the liquid properties of the droplet and the film. However, the retraction velocity is a function of film thickness, droplet radius, and the ratio of liquid properties. This also reinforces the former conclusion that the deformation transition limit is independent of the impact We number.

For the impact of droplet in a deep pool, a model with a lower horizontal spread of the droplet and film (characterized by a low spread ratio - see Sec. 3.2.3) at the maximum penetration depth is considered. By comparing the maximum penetration depth from experiment data and theoretical calculation, we can conclude that the model agrees fairly well with our experimental results.

For the new impact phenomenon *Late merging-II*, several experiments were performed to establish that it only exists in the case of droplet impact on a film of different liquid (i.e., a two-liquid system). We provide a possible reason based on the capillary wave theory to explain this phenomena. However, further studies are required to correctly identify the physical mechanisms that drive this phenomena .

4.2　Future Work

The studies presented here in this thesis are not sufficient to forecast all the possible outcomes of droplet impact on liquid films at any given conditions. Several interesting problems are proposed here for future studies to expand up on the current thesis.

1) We have investigated the impact results from nine different droplet-film experiment liquid combinations, and generalized the impact result regime graph. More experimental and numerical work can be done to identify a generalized regime graph.

2) As for the initial limit, the dependency of the critical penetration velocity on both the droplet and the film liquid proprieties remains unknown. This is mostly due to the lack of understanding of the dynamics of the gas layer that gets trapped between the droplet and the film. Hence we need to further study the behavior of this gas layer and its break down mechanism. Future work should also focus on identifying the dependence of fluid properties on the critical ratio of retraction velocities of the droplet and the film corresponding to the deformation transition limit.

Appendix A

Additional Experimental Figures

This Appendix attaches additional experimental figures from the experiment of the droplet impact on liquid film in both single-liquid systems and two-liquid systems.

Figure A.1 shows the impact outcome regime graphs in single-liquid systems of Alkane group (C10 and C14). Three different impact outcomes are shown here, *bouncing*, *earlymerging* and *latemerging*, which are generalized in the former analysis. Similar transition boundaries between different impact outcomes are also shown here, with the shifting in the transition boundaries discussed in each analysis parts.
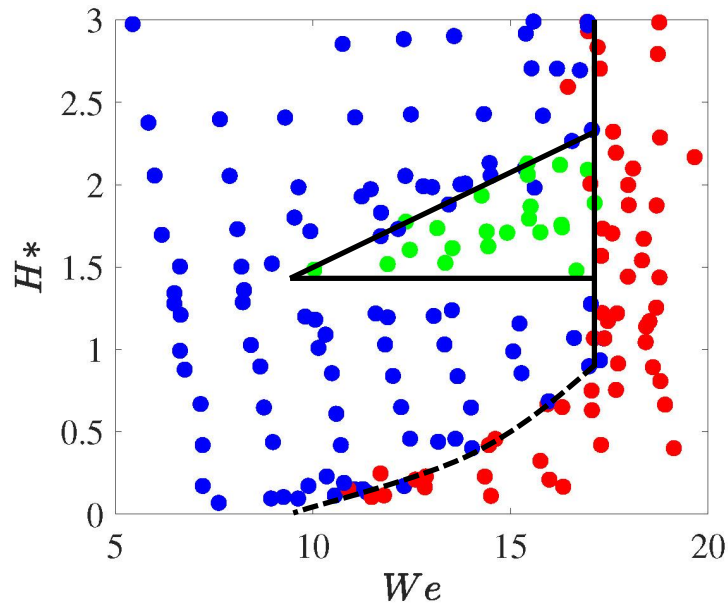
Figure A.2 shows the impact outcome regime graphs in two-liquid systems of Alkane group. Four different impact outcomes are shown in the regime graphs- *bouncing*, *earlymerging*, *latemerging* and *latemerging − II*. The transition boundaries in the regime graph of two-liquid system are similar to the boundaries in single-liquid systems. As we have shown in this thesis, an unique impact outcome *latemerging − II* occurs only in the two-liquid system.

Moreover, figure A.3 shows the impact outcome regime graphs in two-liquid systems for S3 (droplet) to S20 (film). In this regime graph there is no *latemerging* cases, so two of the transition boundaries-deformation transition limit and deep pool limit are not applied in this case. The possible reason for the lacking of the *latemerging* case is that the viscosity of the film is comparatively high, so the slope of the maximum penetration depth with Weber number is lower than other experiment liquid combinations. The potential deep pool limit would become almost horizontal and finally collapse with the deformation transition limit. Thus, there are only three impact outcomes shown in this two-liquid systems other than four different impact outcomes.

The additional regime graphs attached in this appendix have the same boundaries as introduced in chapter 3. Also, the experimental data from these liquid combination have been proved to fit the analysis as discussed and shown.
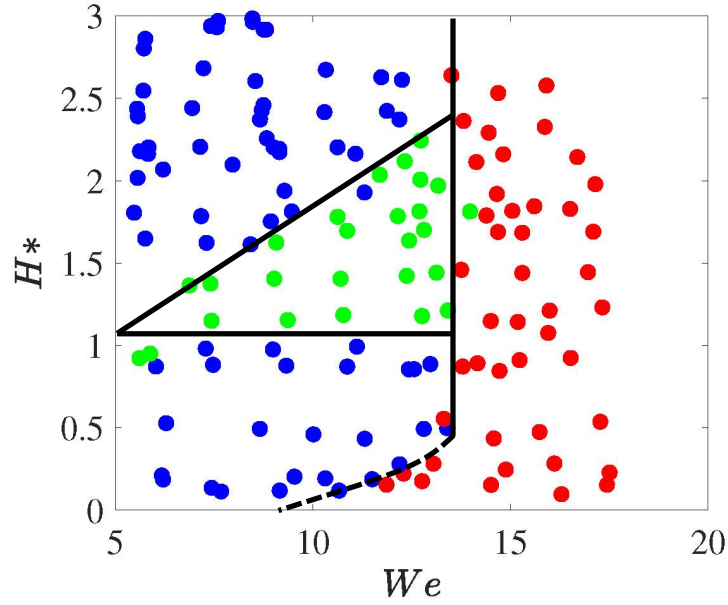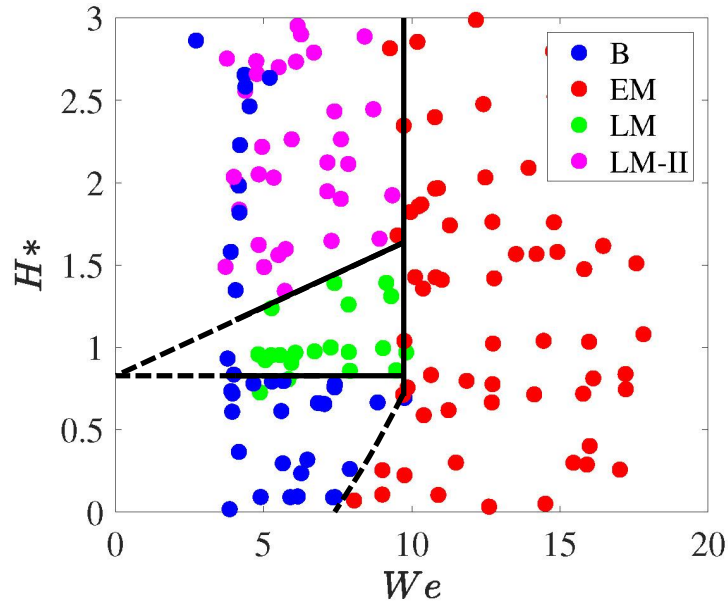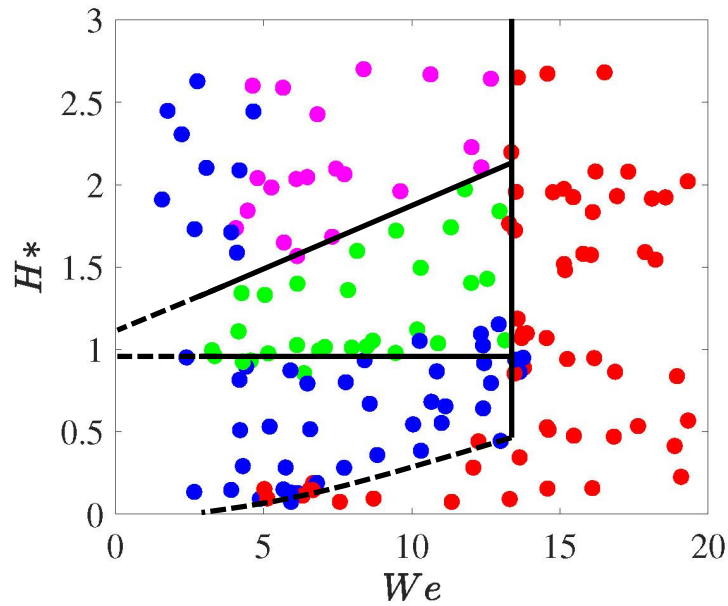
(a)

(b)

Figure A.1: The regime graph of droplet impact outcomes in single-liquid systems for (a) C10 and (b) C14. Three different impact outcomes are shown in the figure: bouncing in blue, early merging in rad and late merging in green.

(a)

(b)

Figure A.2: The regime graph of droplet impact outcomes in two-liquid systems for (a) C10 to C14 and (b) C14 to C10. Four different impact outcomes are shown in the figure: bouncing in blue, early merging in rad, late merging in green and late merging-II in pink.
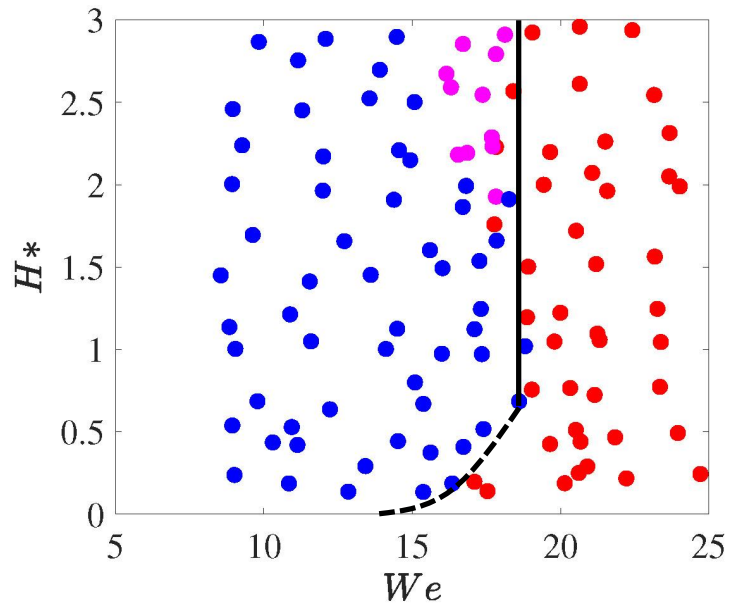
Figure A.3: The regime graph of droplet impact outcomes in two-liquid systems for S3 (droplet) to S20 (film). Only three different impact outcomes are shown in the figure: bouncing in blue, early merging in rad and late merging-II in pink.

Bibliography

[1] X. Wang, M. Jiang, Z. Zhou, J. Gou, and D. Hui, "3d printing of polymer matrix composites: A review and prospective," *Composites Part B: Engineering*, vol. 110, pp. 442–458, 2017.

[2] P. Calvert, "Inkjet printing for materials and devices," *Chemistry of materials*, vol. 13, no. 10, pp. 3299–3305, 2001.

[3] A. Feuerstein, J. Knapp, T. Taylor, A. Ashary, A. Bolcavage, and N. Hitchman, "Technical and economical aspects of current thermal barrier coating systems for gas turbine engines by thermal spray and ebpvd: a review," *Journal of Thermal Spray Technology*, vol. 17, no. 2, pp. 199–213, 2008.

[4] J. Mostaghimi, S. Chandra, R. Ghafouri-Azar, and A. Dolatabadi, "Modeling thermal spray coating processes: a powerful tool in design and optimization," *Surface and Coatings Technology*, vol. 163, pp. 1–11, 2003.

[5] S. D. Aziz and S. Chandra, "Impact, recoil and splashing of molten metal droplets," *International journal of heat and mass transfer*, vol. 43, no. 16, pp. 2841–2857, 2000.

[6] A. M. Worthington, "On the forms assumed by drops of liquids falling vertically on a horizontal plate," *Proceedings of the royal society of London*, vol. 25, pp. 261–272, 1876.

[7] I. Hutchings, G. Martin, and S. Hoath, "High speed imaging and analysis of jet and drop formation," *Journal of Imaging Science and Technology*, vol. 51, no. 5, pp. 438–444, 2007.

[8] A. Castrejón-Pita, J. Castrejón-Pita, and I. Hutchings, "Experimental observation of von kármán vortices during drop impact," *Physical Review E*, vol. 86, no. 4, p. 045301, 2012.

[9] K. R. Langley, E. Q. Li, and S. T. Thoroddsen, "High-speed interferometry under impacting drops," in *The Micro-World Observed by Ultra High-Speed Cameras*, pp. 321–341, Springer, 2018.

[10] N. Ninomiya and K. Iwamoto, "Piv measurement of a droplet impact on a thin fluid layer," in *AIP Conference Proceedings*, vol. 1428, pp. 11–17, American Institute of Physics, 2012.

[11] D. B. Hann, A. V. Cherdantsev, A. Mitchell, I. McCarthy, B. N. Hewakandamby, and K. Simmons, "A study of droplet impact on static films using the bb-lif technique," *Experiments in Fluids*, vol. 57, no. 4, p. 46, 2016.

[12] K. Haller, Y. Ventikos, D. Poulikakos, and P. Monkewitz, "Computational study of high-speed liquid droplet impact," *Journal of Applied Physics*, vol. 92, no. 5, pp. 2821–2828, 2002.

[13] S. Thoroddsen, T. Etoh, and K. Takehara, "High-speed imaging of drops and bubbles," *Annu. Rev. Fluid Mech.*, vol. 40, pp. 257–285, 2008.

[14] R. Ford and C. Furmidge, "Impact and spreading of spray drops on foliar surfaces," *Soc Chem Ind Monogr*, vol. 25, pp. 417–32, 1967.

[15] S. Chandra and C. Avedisian, "On the collision of a droplet with a solid surface," *Proceedings of the Royal Society of London. Series A: Mathematical and Physical Sciences*, vol. 432, no. 1884, pp. 13–41, 1991.

[16] H. Fukanuma and A. Ohmori, "Behavior of molten droplets impinging on flat surfaces," tech. rep., ASM International, Materials Park, OH (United States), 1994.

[17] T. Bennett and D. Poulikakos, "Splat-quench solidification: estimating the maximum spreading of a droplet impacting a solid surface," *Journal of Materials Science*, vol. 28, no. 4, pp. 963–970, 1993.

[18] F. H. Harlow and J. P. Shannon, "The splash of a liquid drop," *Journal of Applied Physics*, vol. 38, no. 10, pp. 3855–3866, 1967.

[19] C. Josserand and S. T. Thoroddsen, "Drop impact on a solid surface," *Annual review of fluid mechanics*, vol. 48, pp. 365–391, 2016.

[20] R. L. Vander Wal, G. M. Berger, and S. D. Mozes, "The splash/non-splash boundary upon a dry surface and thin fluid film," *Experiments in fluids*, vol. 40, no. 1, pp. 53–59, 2006.

[21] D. Bartolo, C. Josserand, and D. Bonn, "Retraction dynamics of aqueous drops upon impact on non-wetting surfaces," *Journal of Fluid Mechanics*, vol. 545, pp. 329–338, 2005.

[22] X. Deng, F. Schellenberger, P. Papadopoulos, D. Vollmer, and H.-J. Butt, "Liquid drops impacting superamphiphobic coatings," *Langmuir*, vol. 29, no. 25, pp. 7847–7856, 2013.

[23] C. Antonini, F. Villa, I. Bernagozzi, A. Amirfazli, and M. Marengo, "Drop rebound after impact: The role of the receding contact angle," *Langmuir*, vol. 29, no. 52, pp. 16045–16050, 2013.

[24] M. Smith and V. Bertola, "Particle velocimetry inside newtonian and non-newtonian droplets impacting a hydrophobic surface," *Experiments in Fluids*, vol. 50, no. 5, pp. 1385–1391, 2011.

[25] A. L. Yarin, "Drop impact dynamics: splashing, spreading, receding, bouncing...," *Annu. Rev. Fluid Mech.*, vol. 38, pp. 159–192, 2006.

[26] K.-L. Pan and C. K. Law, "Dynamics of droplet–film collision," *Journal of fluid mechanics*, vol. 587, pp. 1–22, 2007.

[27] X. Tang, A. Saha, C. K. Law, and C. Sun, "Bouncing-to-merging transition in drop impact on liquid film: Role of liquid viscosity," *Langmuir*, vol. 34, no. 8, pp. 2654–2662, 2018.

[28] M.-J. Thoraval, K. Takehara, T. G. Etoh, S. Popinet, P. Ray, C. Josserand, S. Zaleski, and S. T. Thoroddsen, "von kármán vortex street within an impacting drop," *Physical review letters*, vol. 108, no. 26, p. 264506, 2012.

[29] G. Cossali, M. Marengo, A. Coghe, and S. Zhdanov, "The role of time in single drop splash on thin film," *Experiments in Fluids*, vol. 36, no. 6, pp. 888–900, 2004.

[30] J. B. Lee, D. Derome, R. Guyer, and J. Carmeliet, "Modeling the maximum spreading of liquid droplets impacting wetting and nonwetting surfaces," *Langmuir*, vol. 32, no. 5, pp. 1299–1308, 2016.

[31] E. Berberović, N. P. van Hinsberg, S. Jakirlić, I. V. Roisman, and C. Tropea, "Drop impact onto a liquid layer of finite thickness: Dynamics of the cavity evolution," *Physical Review E*, vol. 79, no. 3, p. 036306, 2009.

[32] B. Wang, C. Wang, Y. Yu, and X. Chen, "Spreading and penetration of a micro-sized water droplet impacting onto oil layers," *Physics of Fluids*, vol. 32, no. 1, p. 012003, 2020.

[33] J. C. Russ, "Image processing," in *Computer-assisted microscopy*, pp. 33–69, Springer, 1990.

[34] S. Wang, F. Ge, and T. Liu, "Evaluating edge detection through boundary detection," *EURASIP Journal on Advances in Signal Processing*, vol. 2006, no. 1, p. 076278, 2006.

[35] Z. Hocenski, S. Vasilic, and V. Hocenski, "Improved canny edge detector in ceramic tiles defect detection," in *IECON 2006-32nd Annual Conference on IEEE Industrial Electronics*, pp. 3328–3331, IEEE, 2006.

[36] J. Canny, "A computational approach to edge detection," *IEEE Transactions on pattern analysis and machine intelligence*, no. 6, pp. 679–698, 1986.

[37] W. He and K. Yuan, "An improved canny edge detector and its realization on fpga," in *2008 7th World Congress on Intelligent Control and Automation*, pp. 6561–6564, Ieee, 2008.